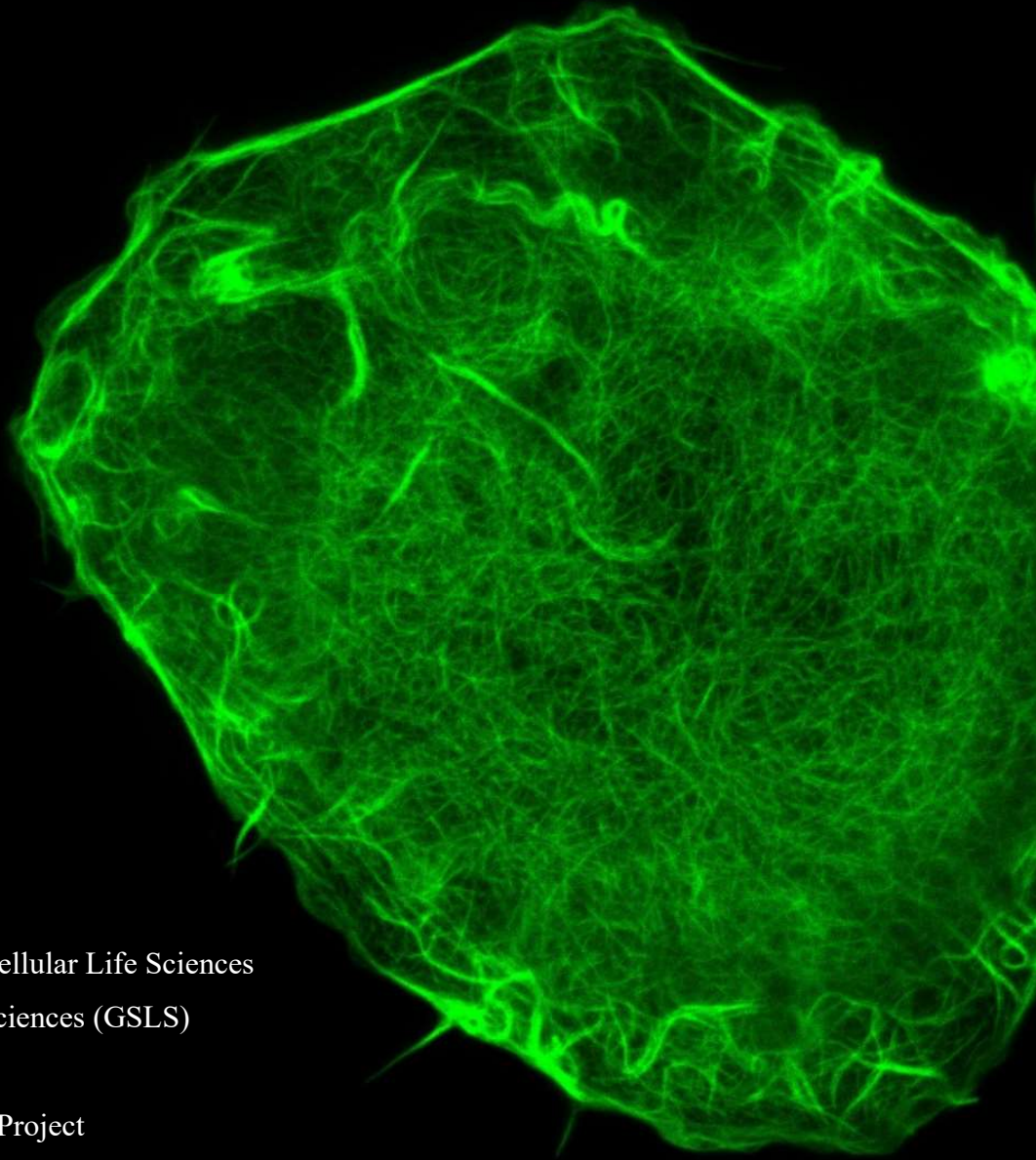


# The Cortical Actin Cytoskeleton: A Modulator of Plasma Membrane Protein Diffusion



**T.J. van der Linden**

**ID: 6967744**

Master's Molecular and Cellular Life Sciences

Graduate school of Life Sciences (GSLs)

Utrecht University

Master's Minor Research Project

Examiner: Dr. Erdinç Sezgin

Cell Signalling, Immunity and Nanoimaging Laboratory (SciLifeLab)

Second Examiner: Dr. Harold MacGillavry

Department of Biology (Utrecht University)

28<sup>th</sup> of February, 2022

## Table of Contents

ABBREVIATIONS.....	3
LAYPERSON’S SUMMARY .....	4
ABSTRACT .....	5
BACKGROUND.....	6
RESEARCH AIMS .....	9
METHODS.....	9
<i>Cloning of Plasmids</i> .....	9
<i>Cell Culture and Transfection</i> .....	10
<i>Cell labelling and Drug Treatment</i> .....	10
<i>GPMV production</i> .....	11
<i>Data Acquisition</i> .....	12
<i>Data Analyses</i> .....	13
RESULTS.....	15
<i>Cytochalasin D and CK666 disrupt the actin cytoskeleton</i> .....	15
<i>GPMVs do not have the cortical actin cytoskeleton</i> .....	18
<i>Protein membrane organisation changes when drugs are applied</i> .....	18
<i>The actin cytoskeleton affects membrane diffusion differently between cell lines</i> .....	25
<i>Changes in diffusion coefficient are not necessarily linked with changes of the anomalous factor</i> .....	28
DISCUSSION .....	30
OUTLOOK.....	35
CONCLUSION .....	37
REFERENCES.....	38

## ABBREVIATIONS

Table 1. Table containing abbreviations used in the present work. The left column contains the abbreviations and the right column contains the full form.

<b>Chemicals and drugs</b>	
CytD	Cytochalasin D
DMEM	Dulbecco's Modified Eagle Medium
DMEM/F12	Dulbecco's Modified Eagle Medium/Nutrient Mixture F-12
DMSO	Dimethyl Sulfoxide
DTT	1,4-dithiothreitol
FBS	Fetal Bovine Serum
NEM	N-ethylmaleimide
PFA	Paraformaldehyde
<b>Proteins and lipids</b>	
Arp2/3	Actin Related Protein complex 2/3
Atto647N-DOPE	Atto647N-1,2-dioleoyl-sn-glycero-3-phosphoethanolamine
Atto647N-SM	Sphingomyelin
BCR	B Cell Receptor
CD4-mNG	mNeonGreen labelled CD4
CD59-mNG	mNeonGreen labelled CD59
DOPE	1,2-dioleoyl-sn-glycero-3-phosphoethanolamine
DOPE-PEG-ASR	Abberior Star Red-labelled DOPE with a polyethylene glycol linker
ERM	Ezrin, Radixin And Moesin
GPI-APs	Glycophosphatidylinositol-Anchored Proteins
Lck	Lymphocyte-Specific Protein Tyrosine Kinase
Lck-SH4-mNG	mNeonGreen labelled SH4 domain of lymphocyte-specific protein tyrosine kinase
LifeAct-mNG	mNeonGreen labelled LifeAct
mNG	mNeonGreen
PS	Phosphatidylserine
<b>Technology-related abbreviations</b>	
ACF	Autocorrelation Function
CLSM	Confocal Laser Scanning Microscope
<i>D</i>	Diffusion Coefficient
FCS	Fluorescence Correlation Spectroscopy
GPMV	Giant Plasma Membrane Vesicles
STED	Stimulated-Emission-Depletion
$\alpha$	Anomalous Factor
<b>Cell types</b>	
CHO	Chinese Hamster Ovary
NRK	Normal Rat Kidney

## LAYPERSON'S SUMMARY

The plasma membrane is crucial to the life of a cell. It separates the intra- and extracellular spaces and has crucial roles in cellular communication and migration. All cell membranes are composed of a very thin film of phospholipids in which proteins are embedded. This arrangement causes cell membranes to be highly dynamic and fluid structures.

It has long been thought that this fluidic nature enables molecules to freely diffuse over the plasma membrane surface. This would result in a homogenous distribution of all membrane components along the membrane surface. However, a large number of studies have shown this not to be the case for many of the molecules residing within the plasma membrane. One of the mechanisms that prevents a free diffusion of membrane molecules is driven by the cortical actin cytoskeleton. This is a dense, mesh-like structure that is tethered to the intracellular side of the plasma membrane. The cortical actin cytoskeleton functions to define cell morphology and provide resistance against mechanical stress. Recently, this structure has also been identified to act as a barrier to membrane molecules, resulting in the compartmentalisation of the plasma membrane. Within the formed membrane compartments, molecules are thought to diffuse freely. However, "hopping over" the cortical actin barrier requires more energy, preventing membrane molecules from freely doing so. Hence, membrane molecules may become stuck within such compartments, leading to a restriction of their movement along the plasma membrane.

Currently, there is only a limited understanding of the role of the cortical actin cytoskeleton on membrane molecule diffusion. The plasma membrane compartmentalisation has, however, been linked with cancer, cardiovascular disease and immune cell functionality. Hence, it is of great importance to have a full comprehension of this topic. Up until now, most of the studies regarding the role of the cortical actin cytoskeleton on membrane molecule diffusion have investigated only a limited range of molecules. Hence, the present work has aimed to elucidate the role of the cortical actin cytoskeleton on the diffusion of a large range of membrane proteins, using advanced microscopy techniques.

The present work measured the diffusion of inner membrane leaflet-anchored proteins, transmembrane proteins and outer membrane leaflet-anchored proteins. In cell-derived membrane structures that completely lack any actin cytoskeletal structures, these proteins diffused significantly faster. This suggests the actin cytoskeleton to affect the diffusion of all of these proteins. However, in live cells that had been treated with actin cytoskeleton-disrupting drugs, this effect was shown to be largest for inner membrane leaflet-anchored proteins. Additionally, the cortical actin cytoskeleton has been shown to have cell type-specific effects on the diffusion of membrane molecules. The results presented in this study thereby highlight the importance and complexity of the cortical actin cytoskeletal mechanisms of modulating membrane protein diffusion.

## ABSTRACT

The diffusion dynamics of plasma membrane proteins and lipids are highly important to the health and functioning of cells. The cortical actin cytoskeleton has been suggested to be strongly associated with membrane diffusion, as it has been shown to induce membrane compartmentalisation. However, previous studies have investigated its effect on membrane diffusion on only a limited range of membrane molecules. Therefore, this study has aimed to elucidate the role of the cortical actin cytoskeleton on the diffusion of inner leaflet-anchored proteins, transmembrane proteins and GPI-anchored proteins (GPI-APs) in the plasma membrane. Using confocal imaging and FCS, the membrane organisation and diffusion of these membrane proteins were measured in live cells treated with the cytoskeleton disrupting drugs CK666 and Cytochalasin D (CytD), and in actin cytoskeleton-free giant plasma membrane vesicles (GPMVs). These measurements have found the actin cytoskeleton to play a confining role in the diffusion of the three classes of proteins measured, as diffusion was much faster in the cell-derived GPMVs than in live cells. In live cells treated with CK666 and CytD, this effect was shown to be largest for inner leaflet-anchored proteins. Additionally, diffusion was shown to be slower and more affected by cytoskeleton disrupting drugs in CHO cells than in U2OS cells. This strongly suggests there to be cell-specific effects of the cortical actin cytoskeleton on membrane diffusion. The results presented in this study thereby highlight the importance and complexity of the cortical actin cytoskeletal mechanisms of modulating membrane protein diffusion.

## BACKGROUND

The plasma membrane is crucial to the life of a cell and the health of the organism. It has a wide variety of functions, with vital roles in cell signalling processes, transport and host-pathogen interactions (1-3). Throughout the last century, the physicochemical principles of the plasma membrane have been the subject of a great amount of investigation. This has resulted in the formation of various models of membrane biophysics. One of the first scientifically accepted models was proposed in 1935 by Hugh Davson and James Danielli. In this model, two protein layers surround a central phospholipid bilayer to form a so-called lipo-protein sandwich (4). Although numerous modifications have been made throughout its history, it remained the generally accepted model of the plasma membrane's physicochemical properties until the start of the 1970's. However, as biochemical assays and microscopy technologies progressed, our understanding of the plasma membrane improved as well. Subsequently, the lipo-protein sandwich model could no longer adequately support the new findings. This prompted S.J. Singer and G.L. Nicolson to propose the fluid mosaic model in 1972. Here, it is suggested that proteins are partially embedded into the phospholipid bilayer, resulting in the formation of a two-dimensional solution of proteins in a viscous phospholipid bilayer solvent (5).

The fluid mosaic model is not without its flaws, however. A system such as proposed in this model would suggest its processes to be mainly driven by free Brownian diffusion, resulting in a homogeneous, multicomponent environment. However, this has been shown to be largely inaccurate (1). Various mechanisms have been revealed to constrain the lateral motion of membrane molecules, with a heterogeneous membrane organisation as a result (1, 3). One such mechanism has been proposed to be driven by the specific interactions between membrane lipids such as cholesterol with sphingolipids. These preferential interactions have been suggested to induce the formation of highly dynamic membrane nanodomains that are enriched in cholesterol and sphingolipids, referred to as lipid rafts (1, 3, 6-8). Numerous proteins have been shown to contain motifs that mediate their specific binding within lipid rafts, which may indicate that these domains play major roles in cell signalling (3, 6).

Most relevant to this study, however, is the role of the cortical actin cytoskeleton as a major driver of membrane heterogeneity and membrane compartmentalisation. The cortical actin cytoskeleton is a dense mesh-like structure composed of F-actin, of between 100 nm and 500 nm in thickness. It is tethered to the plasma membrane through a high number of interactions with proteins of the ERM family (i.e. ezrin, radixin and moesin) (9). As is the case for all actin-based structures, the formation of the cortical actin cytoskeleton is a careful balancing act of monomeric actin polymerisation and F-actin depolymerisation. This balancing act not only

enables the structure to be stable, but also highly adaptive, which is critical to its functionality. The cortical actin cytoskeleton functions to define cell morphology and provide resistance against mechanical stress. Additionally, cortex remodelling enables endo- and exocytosis, as well as the formation of other actin structures such as filopodia (10, 11). Recently, the cortical actin cytoskeleton has also been heavily studied due to its links with molecular diffusion dynamics and membrane supramolecular arrangements (3, 10-12). Upon adhesion to the plasma membrane, the cortical actin indirectly binds to phosphatidylserine (PS), a charged inner leaflet lipid, through a variety of endogenous actin-binding proteins. This interaction transiently immobilises PS, of which its long saturated acyl chains consequently couple across the membrane bilayer with long acyl chain-containing outer leaflet lipid species (13, 14). Subsequently, domains of long acyl chain lipid species, possibly associated with various lipid-anchored proteins, are formed (3, 13).

Furthermore, the cortical actin cytoskeleton has been suggested to form membrane nanodomains by restricting the diffusion of membrane proteins and phospholipids (1, 2). These findings led to the proposal of the “picket-fence” model. This suggests that the cortical actin filaments (i.e. the fence) interact with transmembrane proteins (i.e. the pickets) to form restrictive barriers that constrain the free Brownian diffusion of other membrane proteins and lipids (figure 1A). Consequently, compartments are formed in which membrane molecules can freely diffuse, while diffusion between such compartments is restricted (figure 1B) (1). The cortical actin cytoskeleton has, indeed, recently been demonstrated to be essential in the compartmentalisation of plasma membrane molecules (1, 2). For example, diffusion of phospholipids was shown to be greatly affected by the Actin Related Protein complex 2/3 (Arp2/3), a known regulator of the cortical actin meshwork branching. Arp2/3 inhibition led to an increased phospholipid diffusion and compartmentalisation was no longer observed. This strongly suggests the free Brownian diffusion of phospholipids in the plasma membrane to be restricted by cortical actin branching (1). Further studies have found the diffusion of various fluorescent lipid analogues, including Atto647N-1,2-dioleoyl-sn-glycero-3-phosphoethanolamine (Atto647N-DOPE) and Atto647N-sphingomyelin (Atto647N-SM) to be constrained by the cortical actin cytoskeleton (1, 2). Additionally, the glycosphosphatidylinositol-anchored protein (GPI-AP) Lypd6 was found to have cortical actin-dependent alterations in its diffusion dynamics (2).

To enable the characterisation of the fast mobility of membrane molecules, a tool is required that can capture the fast diffusion of molecules. Fluorescence correlation spectroscopy (FCS)

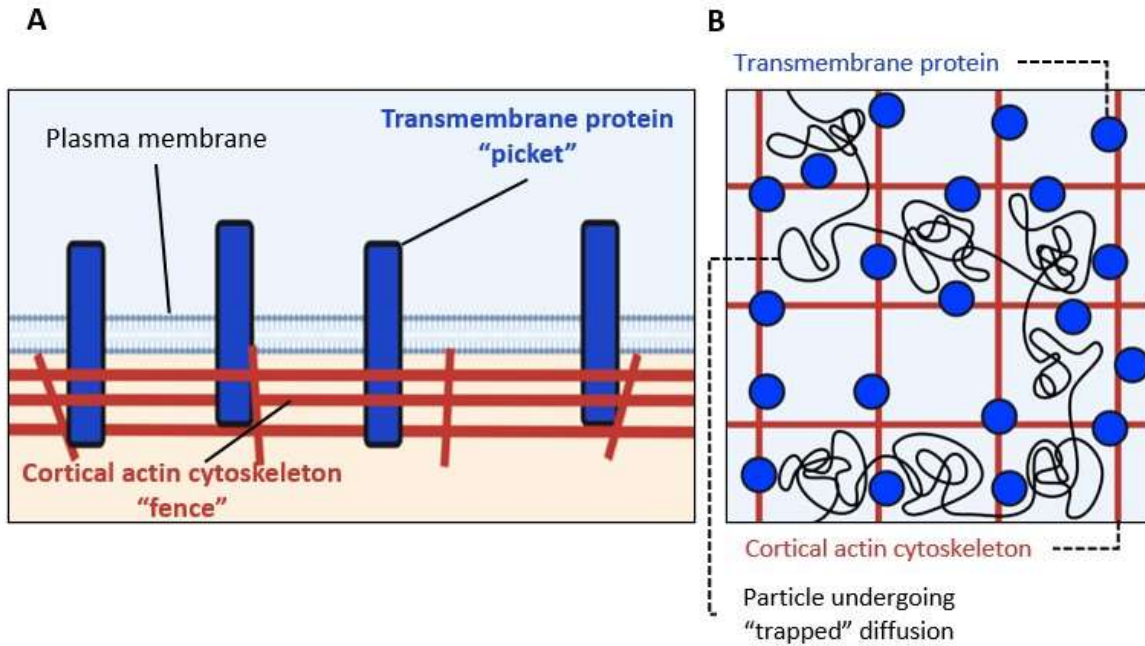


**Figure 1.** Schematic representation of the picket-fence model. This model suggests that (A) the cortical actin filaments (i.e. the fence) interact with transmembrane proteins (i.e. the pickets) to form (B) restrictive barriers that constrain the free Brownian diffusion of other membrane proteins and lipids. Consequently, compartments are formed in which membrane molecules can freely diffuse, while diffusion between such compartments is restricted. In (B), the hop diffusion of a compartmentalised molecule is shown.

is a microscopy-based technique, commonly used to study the diffusion dynamics of fluorescently labelled proteins and lipids. In FCS, the temporal fluctuations in fluorescence intensity caused by the transits of single molecules through the microscope's observation volume is measured. From this data, the autocorrelation function (ACF) is calculated. The resulting autocorrelation curve provides information on the molecule's brightness, concentration and - most importantly - the transit time  $\tau_D$  through the observation volume. Finally, this information enables the calculation of the diffusion coefficient  $D$  (1, 2, 15-18). Therefore, this technique provides an excellent method to study the role of the cortical actin cytoskeleton on the mobility of membrane molecules.

Up until recently, much of the research into the mobility characteristics of membrane proteins has made use of cell-perturbing drugs, such as cytochalasin D (CytD) and CK666. CytD is a fungal toxin that acts as a potent inhibitor of actin polymerization and disrupts actin microfilaments. CK666 is a potent inhibitor of the actin nucleator Arp2/3 and, thereby, causes a reduction in cytoskeletal branching. However, such treatments may potentially result in various off-target effects. Therefore, model membrane systems that contain only the essential elements and provide highly controlled conditions are critical to study the molecular mechanisms that induce hindrances in membrane diffusion (2). Sezgin et al. has presented such



an experimental system called the giant plasma membrane vesicles (GPMVs) (7). These cell-derived membrane vesicles contain most of the natural membrane components, but lack the actin cytoskeleton (2, 7). The role of the actin cytoskeleton can thereby be investigated through the comparison of the diffusion characteristics of live cells against those in GPMVs (2).

A wide range of open questions regarding the role of the cortical actin cytoskeleton in the regulation of molecular diffusion in membranes still remain unanswered. Up until now, research into the regulation of membrane molecule mobility has mainly focussed on phospholipids and GPI-APs (1, 2, 10). GPI-APs are a group of approximately 150 proteins, anchored to the outer leaflet of the plasma membrane through a GPI moiety attached to their C-termini (19). Despite being crucial to the functioning and survival of the cell, they only represent a small fraction of the proteins present on the plasma membrane. The complete influence of the cortical actin cytoskeleton on the mobility of lipids and proteins may have broad implications on cell signalling. Hence, having a full understanding of this topic will greatly impact our understanding of human health and disease (10).

## RESEARCH AIMS

The present study will investigate the diffusion dynamics of the inner membrane leaflet associated lymphocyte-specific protein tyrosine kinase (Lck), the GPI-AP CD59, the transmembrane protein CD4 and of the unsaturated phospholipid DOPE. This will be achieved by applying FCS in the plasma membrane of live CHO and U2OS cells of which the actin cytoskeleton is disrupted through CytD and CK666 treatment, and in GPMV membrane models. We thereby aim to elucidate the role of the cortical actin cytoskeleton on the diffusion of inner leaflet-anchored proteins, transmembrane proteins and GPI-APs in the plasma membrane.

## METHODS

### *Cloning of Plasmids*

To enable the transient expression of fluorescently labelled proteins of interest in CHO and U2OS cells, plasmids encoding LifeAct-mNeonGreen (LifeAct-mNG, Addgene, plasmid #98877), the SH4 domain of the Lymphocyte-specific protein tyrosine kinase-mNeonGreen (Lck-SH4-mNG, internal stock), Endogenous SP-CD4-mNeonGreen (CD4-mNG, internal stock) and CD59-mNeonGreen (CD59-mNG, internal stock) were cloned using the Library Efficiency® DH5 $\alpha$ <sup>TM</sup> Competent Cells (ThermoFisher Scientific<sup>TM</sup>). The transformation of cells with the plasmids was performed with a protocol adapted from the manufacturer's

protocol. In brief, 5 ng DNA in 1  $\mu$ l of MilliQ water was added to 50  $\mu$ l of competent cell solution. The competent cells were then gently mixed and incubated on ice for 30 minutes. Competent cells were subsequently heat-shocked in a 42 °C water bath for 45 seconds, directly after which they were placed on ice for 2 minutes. 500  $\mu$ l S.O.C. medium was then added and cells were then incubated on a shaker at 250 rpm and 37 °C for 1 hour. Finally, cells were spread on plates covered with LB Broth with agar (Miller) (40 g/L, Sigma Aldrich) supplemented with either 100  $\mu$ g/ml ampicillin or 50  $\mu$ g/ml kanamycin. Plates were then left to incubate overnight at 37 °C.

The following day, colonies were picked based on size, and grown overnight in 100 mL LB broth (Miller) (25 g/L, Sigma Aldrich) supplemented with either 100  $\mu$ g/ml ampicillin or 50  $\mu$ g/ml kanamycin. Plasmids were isolated using the ZymoPURE II Plasmid Midiprep Kit (Zymo Research), according to manufacturer's protocol. DNA yield was measured via Nanodrop, using elution buffer as the reference control.

#### *Cell Culture and Transfection*

Chinese Hamster Ovary (CHO, RRID: CVCL\_0213) cells were grown in Dulbecco's Modified Eagle Medium/Nutrient Mixture F-12 (DMEM/F12) with L-glutamine, 15 mM HEPES and phenol red (ThermoFisher Scientific™), supplemented with 10% Fetal Bovine Serum (FBS, Sigma Aldrich). U2OS (RRID: CVCL\_0042) cells were grown in DMEM without Sodium Pyruvate and with 4.5 g/L D-glucose, L-glutamine, phenol red (ThermoFisher Scientific™), supplemented with 10% FBS. Unless stated otherwise, cells were grown at 37 °C in an atmosphere with 90% relative humidity and 5% CO<sub>2</sub>. For transfection,  $0.15 \times 10^6$  cells were seeded on 6-well plates. The following day, cells were transfected with one of the fluorescent proteins: LifeAct-mNG, Lck-SH4-mNG, CD59-mNG or CD4-mNG. The transfections were performed using Lipofectamine 3000 (ThermoFisher Scientific™), according to an altered version of the manufacturer's protocol. This altered protocol used RPMI-1640 medium (Sigma-Aldrich) to suspend the transfection agents and DNA.

#### *Cell labelling and Drug Treatment*

For confocal imaging and diffusion measurements, cells were seeded in 6-well plates containing 25-mm round coverslips (#1) approximately 24 hours after transfection. Once a confluency of approximately 70% was reached, cells were washed twice with phenol red-free L15 medium (ThermoFisher Scientific™) heated to 37 °C. Directly after, cells were treated

with L15 medium pre-heated to 37 °C supplemented with 100 µM CK666 (Sigma Aldrich) and dimethyl sulfoxide (DMSO, Sigma Aldrich) to a final concentration of 0.4% at cell culture conditions for 1 hour. Alternatively, cells were treated with L15 medium pre-heated to 37 °C supplemented with 5 µM CytD (Sigma Aldrich) and DMSO to a final concentration of 0.26% at cell culture conditions for 30 minutes. As control condition, cells were treated with L15 medium pre-heated to 37 °C. Next, all samples measured with FCS were labelled with a custom designed Abberior Star Red-labelled DOPE with a polyethylene glycol linker (DOPE-PEG-ASR, Abberior) at a concentration of 0.2 µM for 10 minutes at room temperature. The PEG linker connects the lipid headgroup to the fluorescent dye. This type of linkage was shown to significantly reduce dye-induced effects on diffusion properties (20). After the incubation with DOPE-PEG-ASR, cells were washed twice with L15 medium pre-heated to 37 °C to minimise fluorescent signal in solution. Cells were subsequently re-treated with the aforementioned drug solutions, to prevent a reversal of the drug-induced actin cytoskeleton disruption during the experiment. Measurements were performed directly at the start of the second drug treatment. Each cover slip was used for experiments for no longer than 45 minutes, to minimise DOPE-PEG-ASR internalisation and changes in cell morphology due to environmental stress.

Cells expressing LifeAct-mNG were imaged with confocal microscopy, but not measured with FCS. These cells were washed twice with L15 medium pre-heated to 37 °C. They were then treated with the aforementioned CK666 or CytD solutions for 1 hour or for 30 minutes, respectively, at cell culture conditions. Cells were subsequently labelled with NucBlue™ Live ReadyProbes™ Reagent (ThermoFisher Scientific™) according to manufacturer's protocol. Imaging was performed directly after, for no longer than 45 minutes.

### *GPMV production*

Cell-derived GPMVs were produced according to an altered version of the protocol described by Sezgin et al (7). For the production of GPMVs, CHO and U2OS cells were seeded in 6-well plates approximately 24 hours after transfection. The following day, when a confluency of approximately 70-80% had been reached, cells were washed twice with GPMV buffer (10 mM HEPES, 150 mM NaCl, 2 mM CaCl<sub>2</sub>, pH 7.4). For U2OS cells, GPMV buffer supplemented with 2 mM N-ethylmaleimide (NEM, Sigma Aldrich) was subsequently added and cells were incubated at cell culture conditions for no more than 2 hours. CHO cells were found to be incompatible with NEM (figure S1). Therefore, CHO-derived GPMVs were produced through the addition of GPMV buffer supplemented with 3 mM 1,4-dithiothreitol (DTT, Sigma Aldrich) and 25 mM paraformaldehyde (PFA, Sigma Aldrich). CHO cells were

subsequently incubated at cell culture conditions for approximately 1.5 hours. When sufficient amount of GPMVs were produced, GPMV-rich supernatant was transferred to a fresh Eppendorf tube using a wide-orifice pipette tip to prevent shear-stress. GPMVs were subsequently stored at cell culture conditions until further labelling was applied and were stable for multiple hours. Finally, the GPMVs were placed in an 8-well  $\mu$ -Slide with glass bottom (Ibidi) and labelled with DOPE-PEG-ASR at a concentration of 0.05  $\mu$ M immediately before measurements were performed. Measurements did not last for longer than 45 minutes.

### *Data Acquisition*

Confocal imaging and FCS measurements were performed using the Zeiss LSM 780/980 confocal laser scanning microscope (CLSM) equipped with a 40x 1.2 water-immersion objective, connected to the ZEISS ZEN Microscopy Software (version 3.3, Black edition). Blue, green and far-red fluorescence were excited using 405 nm, 488 nm and 633 nm lasers, respectively. Their fluorescent emission was collected in two channels of the 32-channel detector within the spectral windows of 412–490 nm, 490–597 nm and 641–695 nm, respectively. For the confocal imaging, the pinhole parameter was set to one Airy unit. Four times line averaging was applied, with a dynamic range of 8 bits (i.e. 256 grey value units). Before each image was taken, the focal plane was adjusted until the cell's basal membrane or the GPMV's equatorial plane were in focus.

Prior to diffusion measurements, a setup calibration was performed. In this process, the pinhole position and the correction collar of the objective were calibrated using a 10 nM solution of Alexa 488 in water as reference. When performing diffusion measurements in live cells, the Alexa 488 solution was placed on the same type of 25-mm round coverslips (#1) as the cells were grown and measured on. For the diffusion measurements in GPMVs, the Alexa 488 solution was placed on the same 8-well  $\mu$ -Slide as the samples. The calibration was performed by adjusting the focal plane until fluorescent signal was detected. Subsequently, the pinhole size was adjusted using the “fine” option and the correction collar was manually adjusted until the highest signal was achieved. Finally, to enable the calculation of the microscope's observation volume, 5 measurements of 10 seconds were performed with low laser power.

Diffusion measurements in cells were performed on the basal membrane of cells displaying a relatively homogenous membrane protein organisation (examples shown in figure S2-S7). The focal plane was manually adjusted until the highest signal was achieved for the far-red fluorescence (i.e. DOPE-PEG-ASR), as this indicated the plasma membrane to be in focus. FCS

curves were obtained through 5 measurements of 5 seconds at low laser power to prevent photobleaching. Diffusion measurements in GPMVs were obtained in identical fashion, apart from the measurements being performed on the top of the vesicle.

### *Data Analyses*

Confocal images were analysed with ImageJ (21). For colocalization analyses, images were cropped to contain only the area of the image displaying the cover glass interface of the plasma membrane. Colocalization analyses were performed using the JACoP plugin (22). Colocalization analyses results are indicated as the average Pearson's coefficient. Membrane protein cluster sizes were obtained using the built-in "analyze particles" option, after adjusting the threshold to a level in which only protein clusters were selected for analysis. Resulting particle sizes were subsequently tested for normality using the Shapiro-Wilk test, and statistically compared with a two-sided Mann-Whitney U test.

The autocorrelation curves obtained from the measurements in cells and GPMVs were fit and analysed using the FoCuS-point fitting software (23). The correlation function obtained from the FCS data was analysed using the following equation:

$$G_N(\tau) = O_f + G_N(0)[G_{diff}(\tau)G_t(\tau)]$$

In which  $G_N$  represents the autocorrelation at the lag time  $\tau$ ,  $O_f$  represents the offset (here, the offset was fixed to 1),  $G_N(0)$  is the amplitude of the correlation function,  $G_{diff}$  is the diffusion component and  $G_t$  the triplet state. Before the analyses of diffusion measurements of membrane proteins and lipids were performed, the diffusion of the reference sample (i.e. 10 nm solution of Alexa 488 in water) was analysed. Its diffusion time was calculated using  $G_{diff}$ , as described with the following equation, which is designed to analyse the correlation function obtained from intensity fluctuations of three-dimensional diffusion:

$$G_{diff}(\tau) = \sum_{k=1}^{D_s} A_k \left( \left( 1 + \left( \frac{\tau}{\tau_{D_k}} \right)^{\alpha_k} \right)^{-1} \left( 1 + \left( \frac{\tau}{AR_k^2 \tau_{D_k}} \right) \right)^{-\frac{1}{2}} \right),$$

in which  $D_s$  specifies the integer number of diffusing species included in the equation  $k$  (here, this was fixed to 1 for the reference sample).  $A_k$  represents the proportion of each diffusion species to the amplitude of the correlation factor.  $\tau_{D_k}$  represents the lateral diffusion rate of each diffusing species, which is the time taken for the fluorescent molecule to move laterally through the microscope's focal volume.  $\alpha_k$  represents the anomalous factor and the AR represents the aspect ratio of the focal volume. For the correlation curves obtained from measurements of membrane proteins and lipids performed in live cells and GPMVs,  $G_{diff}$  was described with an equation used to study two-dimensional diffusion:

$$G_{diff}(\tau) = \sum_{k=1}^{D_s} A_k \left( \left( 1 + \left( \frac{\tau}{\tau_{D_k}} \right)^{\alpha_k} \right)^{-1} \right)$$

$D_s$  was fixed to 1 in all samples, except the CD4-mNG expressing CHO-derived GPMVs. Here, the autocorrelation curve was more accurately fit when 2 diffusing species were included in the equation. The second diffusing species was not significantly different from luminal CD4-mNG ( $p = 0.54$ , figure S8), suggesting the luminal CD4-mNG to be this secondary diffusing species. For all analyses, the triplet state  $G_t$  is included in the analyses to correct for the effect of the triplet states on the diffusion equation. This is crucial, as the triplet states substantially influence the overall correlation curves.  $G_t$  is described with the following equation:

$$G_t(\tau) = 1 + \sum_{j=1}^{T_s} B_j \cdot \exp(-\tau/\tau_{T_j}), B_j = \frac{T_j}{1-T_j}$$

Here,  $T_s$  specifies the integer number of triplet states  $j$ ,  $\tau_{T_j}$  represents the length of the dark state induced by the triplet state. For Alexa488 and DOPE-PEG-ASR,  $\tau_T$  was fixed to 5 milliseconds. For mNeonGreen,  $\tau_T$  was fixed to 40 milliseconds.

The extracted  $\tau_D$  of the labelled proteins and lipids could subsequently be applied to calculate their diffusion coefficients, using the following equation:

$$D = \frac{d^2}{8 \ln 2 \tau_D}$$

Here,  $D$  is the diffusion coefficient of the fluorescently labelled molecule,  $d$  is the full width at half maximum of the beam waist and  $\tau_D$  is the average transit time of the fluorescently labelled molecule of interest (17, 24). First, using R,  $d$  was calculated by applying the known  $D$  of Alexa 488 in water ( $430 \mu\text{m}^2 \text{s}^{-1}$ ) and the  $\tau_D$  determined from the calibration measurements (25, 26). Subsequently, the  $D$  of the labelled proteins and lipids were calculated by using the calculated observation spot size, using the same equation with experimentally obtained diffusion times. Unless otherwise specified, all quantitative output from diffusion measurements were statistically analysed in R using the `ggpubr` package (27). The obtained values of  $D$  and  $\alpha$  were subsequently tested for normality using the Shapiro-Wilk test. For obtained  $D$  values, comparisons between groups were then performed using either a two-sided T-test if the data was normally distributed, or the two-sided Mann-Whitney U test if the data was not normally distributed. For obtained  $\alpha$ , differences from 1 and in between groups were compared using either a two-sided T-test if the data was normally distributed, or a two-sided Mann-Whitney U test if the data was not normally distributed. Differences in  $D$  or  $\alpha$  between groups (or from 1 for  $\alpha$ ) were considered significant from an arbitrary cut-off value of  $p \leq 0.05$ . Significance is indicated as the Holm-Bonferroni adjusted  $p$  value output provided by `ggpubr`.

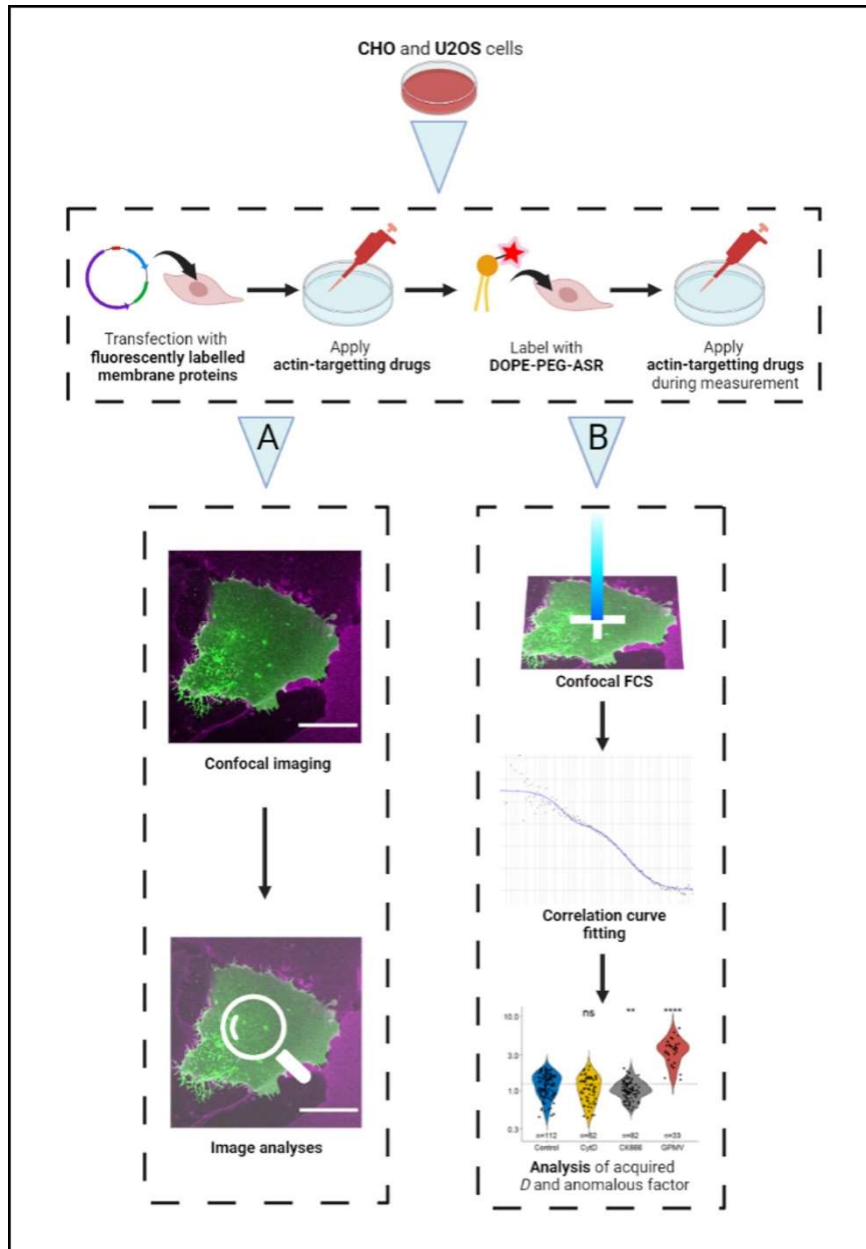


**Figure 2.** A brief overview of the experimental workflow that was used in this study. CHO and U2OS cells were transfected with either Lck-SH4-mNG, CD59-mNG or CD4-mNG. Cells expressing these proteins were subsequently treated with either CytD or CK666 for 30 or 60 minutes, respectively. Cells were then labelled with the lipid analogue DOPE-PEG-ASR and washed to remove unincorporated DOPE-PEG-ASR remaining in-solution. Directly after, cells were treated with either CytD or CK666 for the duration of the subsequent experiment. **(Path A)** Cells were imaged using confocal microscopy. Obtained images were analysed using ImageJ (21). **(Path B)** Membrane diffusion was measured using confocal FCS. The resulting FCS curves were analysed using the FoCuS Point curve fitting software (23), and the acquired diffusion coefficients and anomalous factors were statistically analysed using R.

## RESULTS

### *Cytochalasin D and CK666 disrupt the actin cytoskeleton*

To characterise the role of the cortical actin cytoskeleton in membrane molecule mobility, we treated cells with either CytD or CK666 to alter the dense, mesh-like structure of the actin networks. To identify the effects of these drugs on actin cytoskeletal organisation, U2OS

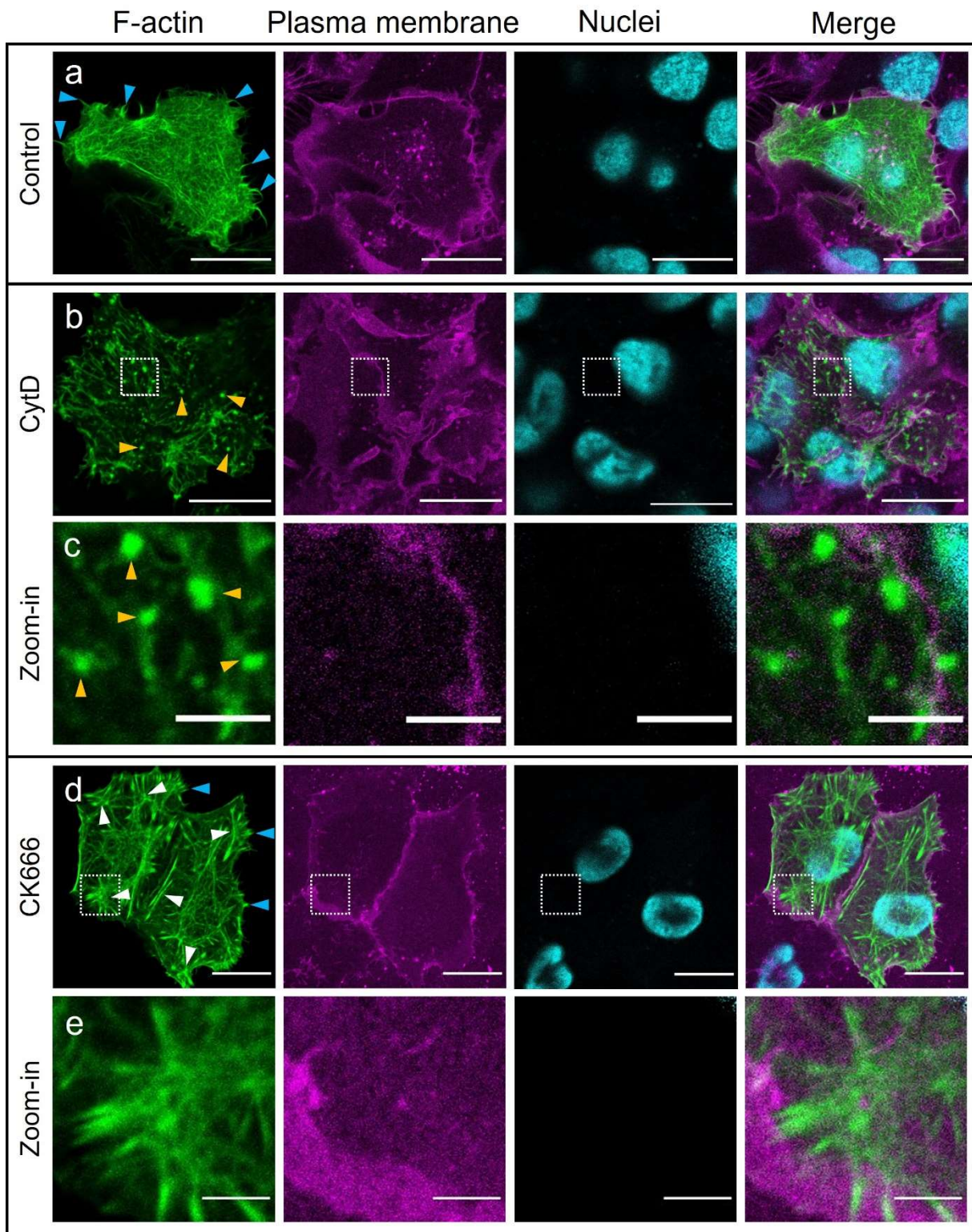


**Figure 3.** Effect of depolymerisation of the actin cytoskeleton by CytD and Arp2/3 complex inhibition by CK666 in U2OS cells. In all conditions, F-actin (green) is labelled with the LifeAct-mNG fluorescent marker, the plasma membrane (magenta) is labelled with DOPE-PEG-ASR and nuclei (cyan) are labelled with NucBlue™ Live ReadyProbes™ Reagent. **a** shows cells in untreated conditions. **b** and **c** show cells treated with 5  $\mu$ M CytD. CytD treated U2OS cells displayed a loss of F-actin filaments and actin aggregates, the latter of which is highlighted in the zoom-in in **c** (examples of aggregates are shown with orange arrows in **b** and **c**). **d** and **e** show cells treated with 100  $\mu$ M CK666. CK666 treated U2OS cells exhibited an increased presence of stress fibres, organised into asters, as highlighted in **e** (examples of stress fibre clusters shown with white arrows in **a** and **d**). Additional CK666 and CytD-related effects were a lack or decrease of filopodia, respectively (examples of filopodia shown with light blue arrows in **a** and **d**). Scale bars in **a**, **b** and **d** are 20  $\mu$ m. Scale bars in **c** and **e** are 4  $\mu$ m.



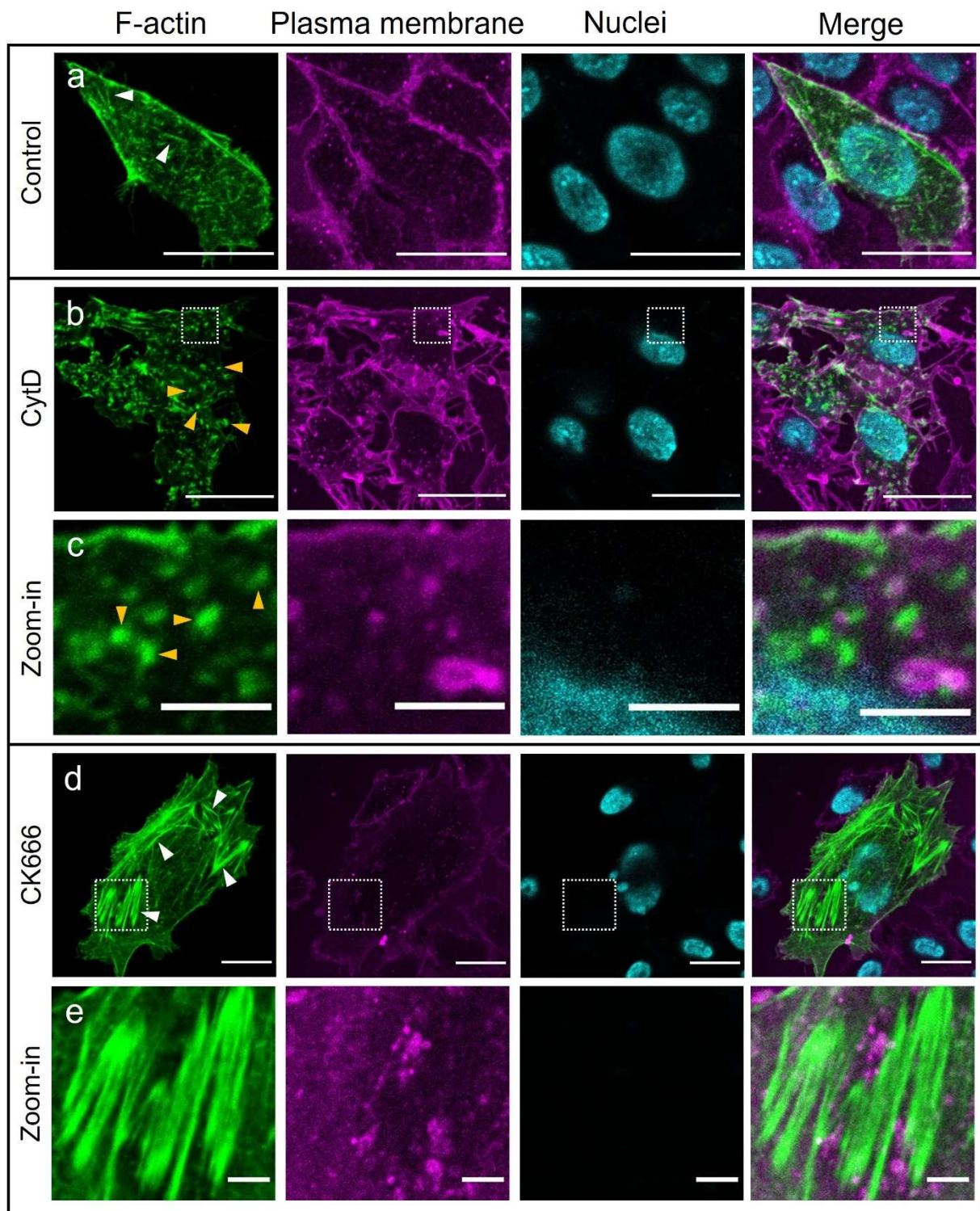


**Figure 4.** Effect of depolymerisation of the actin cytoskeleton by CytD and Arp2/3 complex inhibition by CK666 in CHO cells. In all conditions, F-actin (green) is labelled with the LifeAct-mNG fluorescent marker, the plasma membrane (magenta) is labelled with DOPE-PEG-ASR and nuclei (cyan) are labelled with NucBlue™ Live ReadyProbes™ Reagent. **a** shows cells in untreated conditions. **b** and **c** show cells treated with 5  $\mu$ M CytD. CytD treated CHO cells displayed a loss of F-actin filaments and actin aggregates, the latter of which is highlighted in the zoom-in in **c** (examples of aggregates are shown with orange arrows in **b** and **c**). **d** and **e** show cells treated with 100  $\mu$ M CK666. CHO cells exhibited an increased presence of stress fibres, organised into concentrated bundles of parallel positioned, short fibres, as highlighted in **e** (examples of stress fibre clusters shown with white arrows in **a** and **d**). Scale bars in **a**, **b** and **d** are 20  $\mu$ m. Scale bars in **c** and **e** are 4  $\mu$ m.

and CHO cells expressing LifeAct-mNG (a fluorescently labelled marker with affinity for actin microfilaments commonly used in live-cell imaging) were treated with these drugs and subsequently imaged with confocal microscopy (figure 2). CytD was found to induce major changes in cellular morphology in both cell lines. In accordance to the work by Ayala et al., CytD treatment lead to a loss of F-actin filaments and to the formation of actin aggregates (28). The latter can be observed as amorphous masses throughout the cell (figure 3B-C, 4B-C). CK666 was also shown to have notable effects on the actin cytoskeletal morphology. Both cell lines showed an increased presence of stress fibres. These are higher order cytoskeletal structures, composed of cross-linked actin filaments, indicative of elevated membrane tension (e.g. in response to actin cytoskeletal alterations) (figure 3D-E, 4D-E) (29, 30). Interestingly, however, are the cell-dependent differences in stress fibre morphology. In U2OS cells, many of the stress fibres were shown to be clustered into asters (figure 3E). In contrast, concentrated bundles of short, parallel positioned stress fibres were found in CHO cells (figure 4E). Furthermore, U2OS cells treated with CytD or CK666 displayed either a complete lack of, or a sharp decrease of filopodia (figure 3A, 3B and 3D). In total, these results indicate the cortical actin cytoskeleton to be destabilised or disrupted by CytD and CK666.

#### *GPMVs do not have the cortical actin cytoskeleton*

To confirm the lack of any actin cytoskeleton in GPMVs, we examined actin's organisation in these cell-derived vesicles. GPMVs were isolated from CHO and U2OS cells expressing LifeAct-mNG and imaged with confocal microscopy. In cells, the cortical actin cytoskeleton is clearly visible as a bright, filamentous structure (figure 3A, figure 4A). However, GPMVs did not contain such a structure. Instead, LifeAct-mNG appeared to be homogenously distributed within the vesicles (figure 5). This strongly suggests a lack of actin that is organised into any cytoskeletal structure. Therefore, it can be concluded that GPMVs do not contain any actin cytoskeleton.

#### *Protein membrane organisation changes when drugs are applied*

Before studying the dynamics of membrane proteins, we investigated their organisation within the plasma membrane. We employed three proteins: the SH4 domain of Lck (Lck-SH4), which localizes to the inner membrane leaflet, the GPI-AP CD59, and the transmembrane protein CD4. Lck is an extensively studied immune protein, which is coupled to the inner leaflet

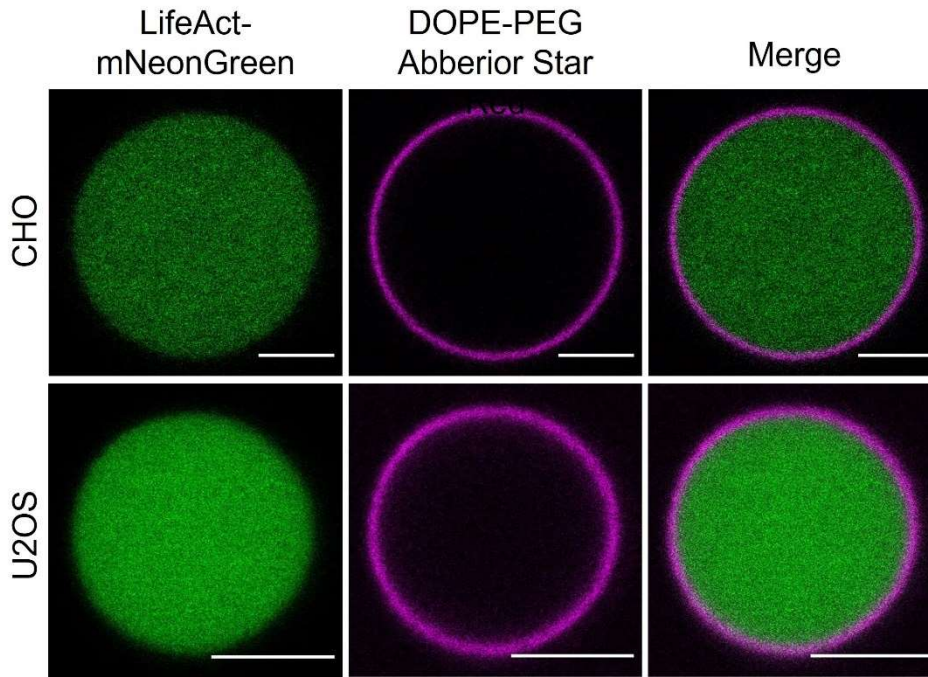


**Figure 5.** Distribution of actin in GPMVs. Confocal images of the equatorial plane of **(top)** CHO-derived and **(bottom)** U2OS-derived GPMVs, expressing LifeAct-mNG and labelled with DOPE-PEG-ASR as a membrane marker. LifeAct-mNG was homogenously distributed within the vesicular lumen, which strongly suggests a complete lack of actin cytoskeletal structures in GPMVs. Scale bar is 5  $\mu\text{m}$ .

of the plasma membrane through the myristoylation and palmitoylation of residues in the SH4 domain (31). CD59 is a glycoprotein that is anchored to the plasma membrane's outer leaflet through a GPI moiety (32). CD4 is a transmembrane glycoprotein, with crucial roles in the adaptive immune response (33). CHO and U2OS cells expressing Lck-SH4-mNG, CD59-mNG or CD4-mNG were labelled with the fluorescent lipid analogue DOPE-PEG-ASR (an unsaturated phospholipid analogue which is mainly located on the outer plasma membrane leaflet). After, cells were treated with either CytD or CK666 and subsequently imaged using confocal microscopy (figure 2). Additionally, GPMVs were produced from identical cells to characterise the organisation of Lck-SH4, CD59 and CD4 in the absence of any actin cytoskeleton.

In untreated U2OS and CHO cells, Lck-SH4-mNG did not distribute homogenously on the plasma membrane (figure 6A-B, figure 7A-B). Namely, large and bright clusters of Lck-SH4-mNG were scattered over the membrane surface. In U2OS cells, these clusters had an average size of 453  $\text{nm}^2$ . They were significantly smaller in CHO cells, however, with an average size of 296  $\text{nm}^2$  ( $p = 0.05$ ). In both cell lines, the Lck-SH4-mNG clusters somewhat co-localised with DOPE-PEG-ASR (U2OS:  $r = 0.42$ ; CHO:  $r = 0.25$ , figure 6B, figure 7B). CK666 treated cells displayed similar organisations. However, when cells were treated with CytD, two cell

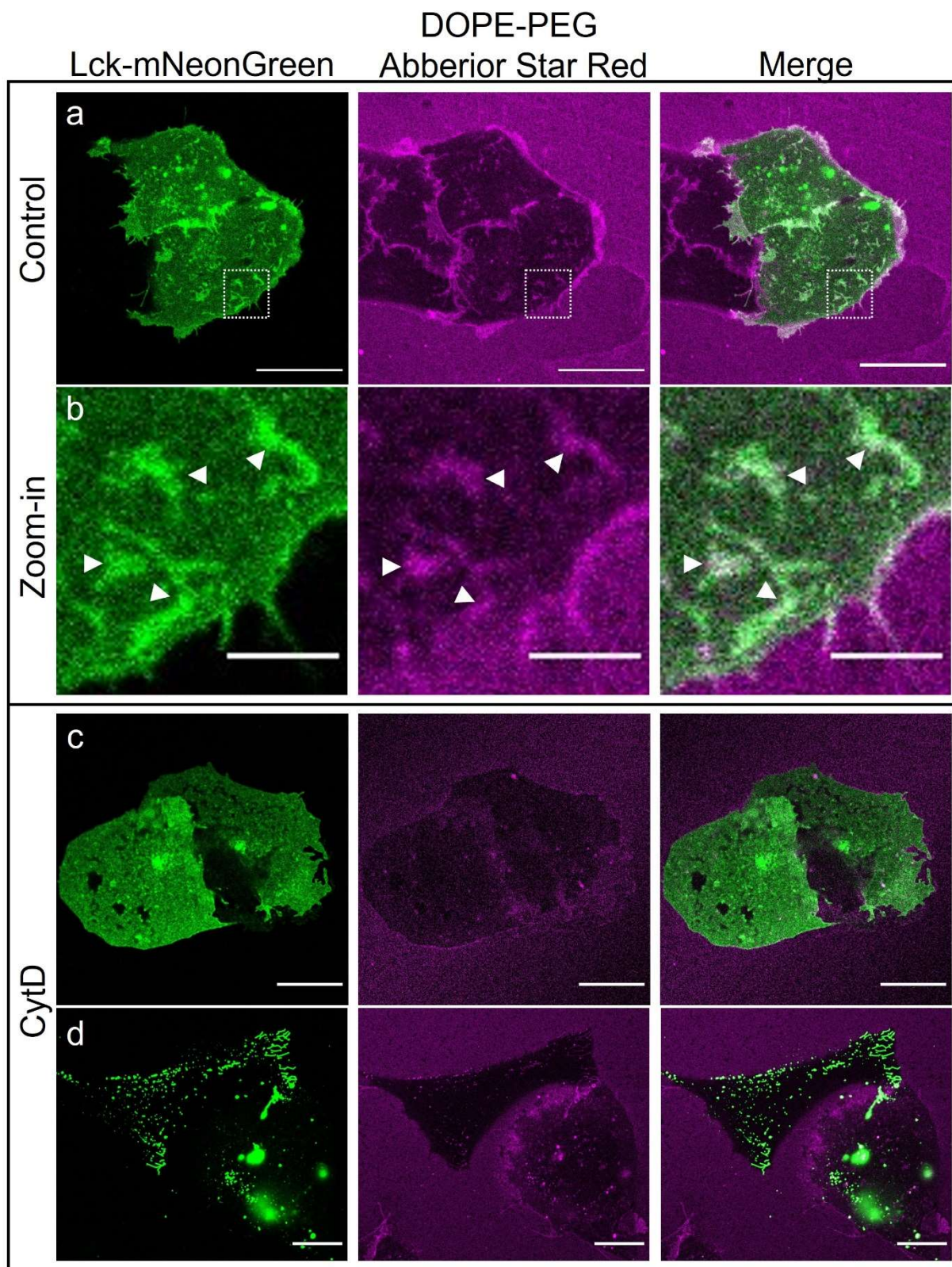


**Figure 6.** Membrane organisation of **Lck-mNeonGreen** in the basal plasma membrane of **U2OS** cells. Figure shows confocal images taken at the cover glass interface of **Lck-mNeonGreen** expressing **U2OS** cells, labelled with **DOPE-PEG-ASR**. **a** and **b** show untreated **U2OS** cells, with **(b)** clusters of **Lck-mNeonGreen** highlighted in the zoom-in. The clusters display co-localisation with **DOPE-PEG-ASR** (examples of colocalizing clusters indicated with white arrows in **b**). **c** and **d** show representative images of **CytD** treated **U2OS** cells. Upon **CytD** treatment, two cell populations were formed. **(c)** One population exhibited a similar membrane distribution of **Lck-SH4-mNG** as in untreated cells, despite having a changed overall cell morphology. **(d)** The other population had large ( $\sim 700 \text{ nm}^2$ ), heterogeneously distributed clusters spread along the membrane. Scale bar in **a**, **c** and **d** is  $20 \mu\text{m}$ . Scale bar in **b** is  $4 \mu\text{m}$ .

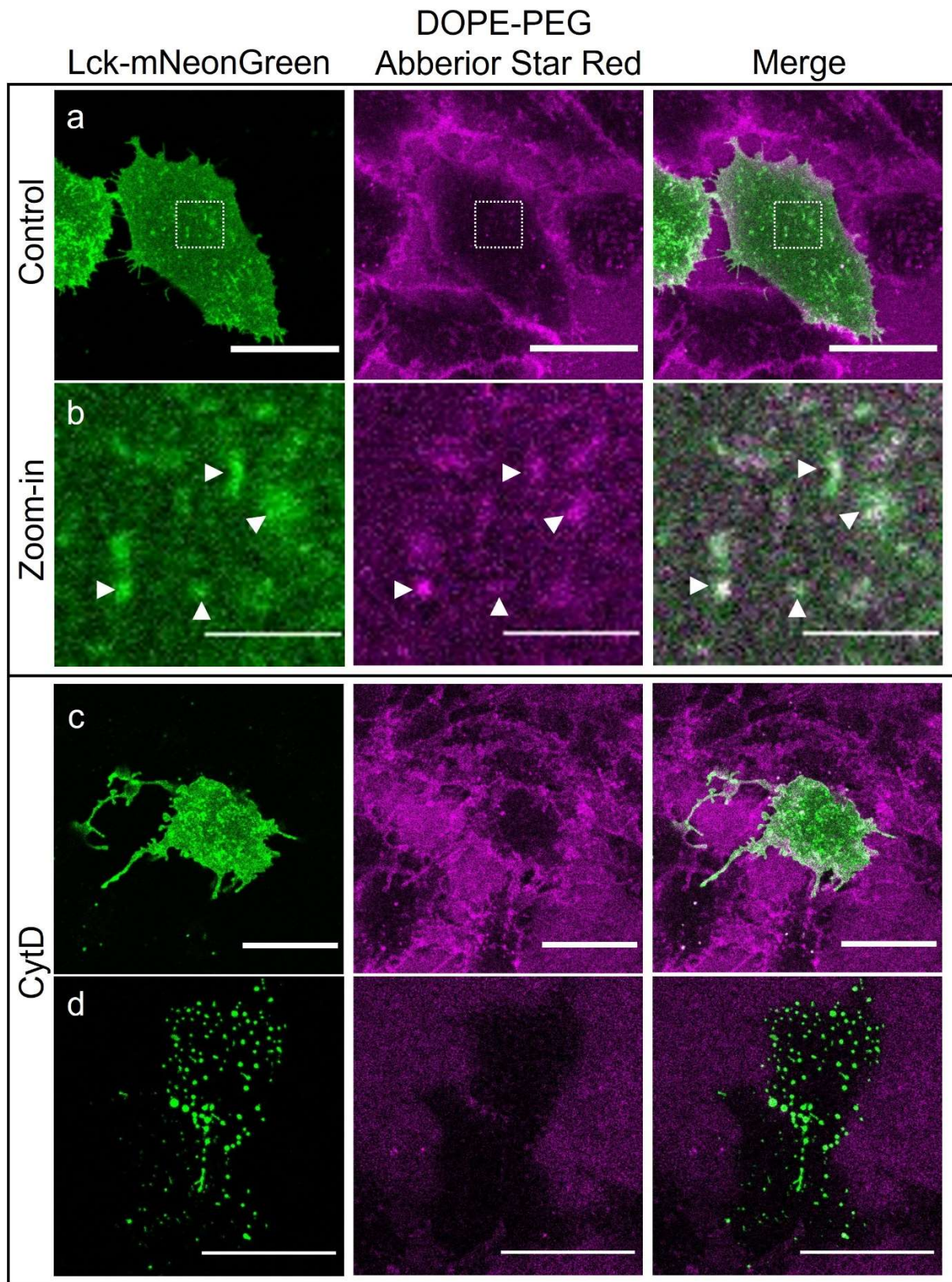


**Figure 7.** Membrane organisation of **Lck-mNeonGreen** in the basal plasma membrane of **CHO** cells. Figure shows confocal images taken at the cover glass interface of Lck-mNeonGreen expressing CHO cells, labelled with DOPE-PEG-ASR. **a** and **b** show untreated CHO cells, with **(b)** clusters of Lck-mNeonGreen highlighted in the zoom-in. The clusters display co-localisation with DOPE-PEG-ASR (examples of colocalizing clusters indicated with white arrows in **b**). **c** and **d** show representative images of CytD treated CHO cells. Upon CytD treatment, two cell populations were formed. **(c)** One population exhibited a similar membrane distribution of Lck-SH4-mNG as in untreated cells, despite having a changed overall cell morphology. **(d)** The other population had large (~620 nm<sup>2</sup>), heterogeneously distributed clusters spread along the membrane. Scale bar in **a**, **c** and **d** is 20  $\mu$ m. Scale bar in **b** is 4  $\mu$ m.

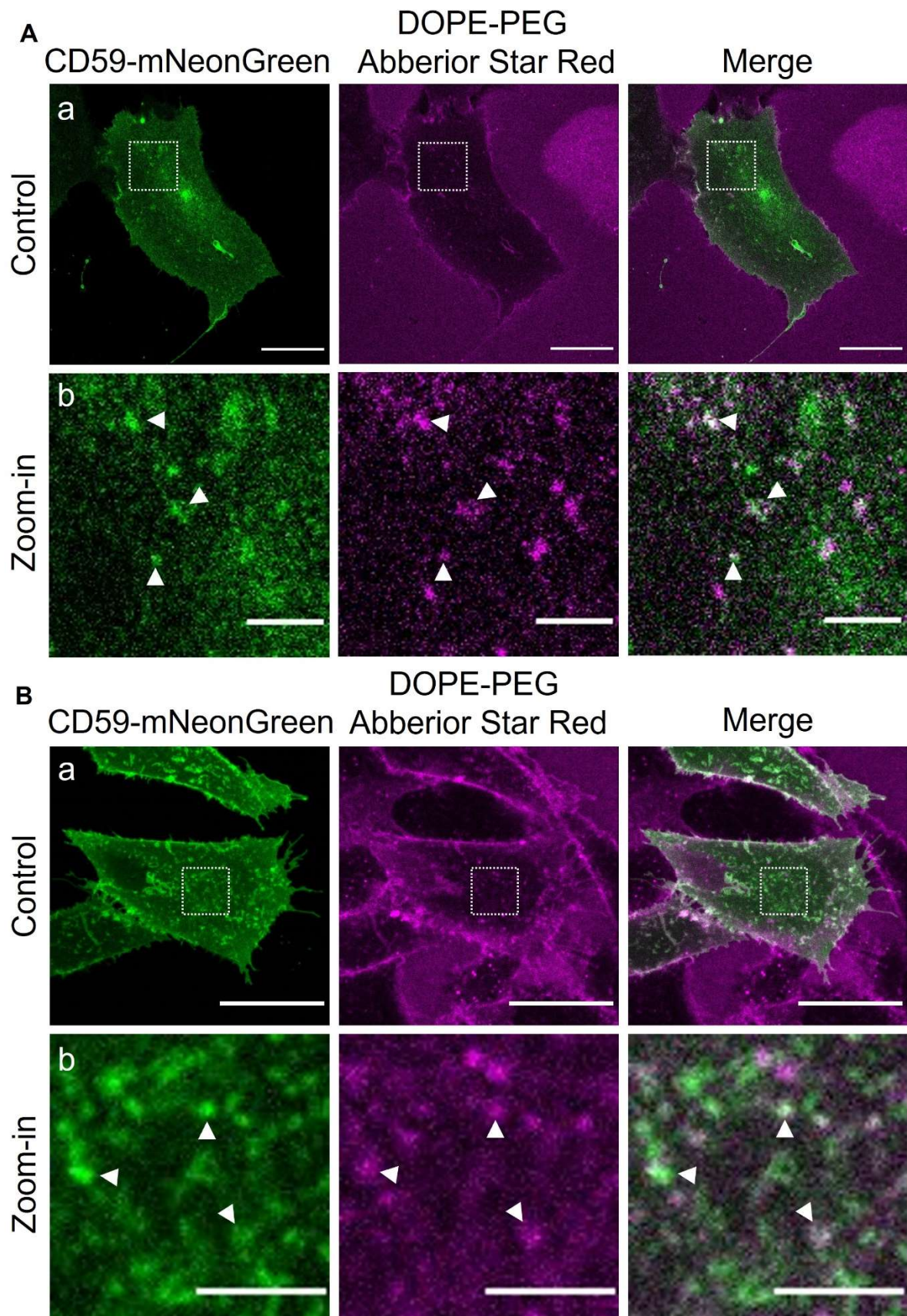


**Figure 8.** Membrane organisation of **CD59-mNeonGreen** on the basal membrane of U2OS and CHO cells. Figure shows representative confocal images taken at the cover glass interface of **(A)** U2OS cells and **(B)** CHO cells expressing CD59-mNeonGreen (green), labelled with DOPE-PEG-ASR (magenta). Both cell lines displayed clusters of CD59 along the membrane surface, which colocalized with DOPE-PEG-ASR (highlighted in **Ab** and **Bb**, examples of clusters indicated with white arrows). CK666 and CytD treatment did not cause a change in membrane organisation from the control (not displayed). Scale bar in **Aa** and **Ba** is 20  $\mu\text{m}$ . Scale bar in **Ab** and **Bb** is 4  $\mu\text{m}$ .

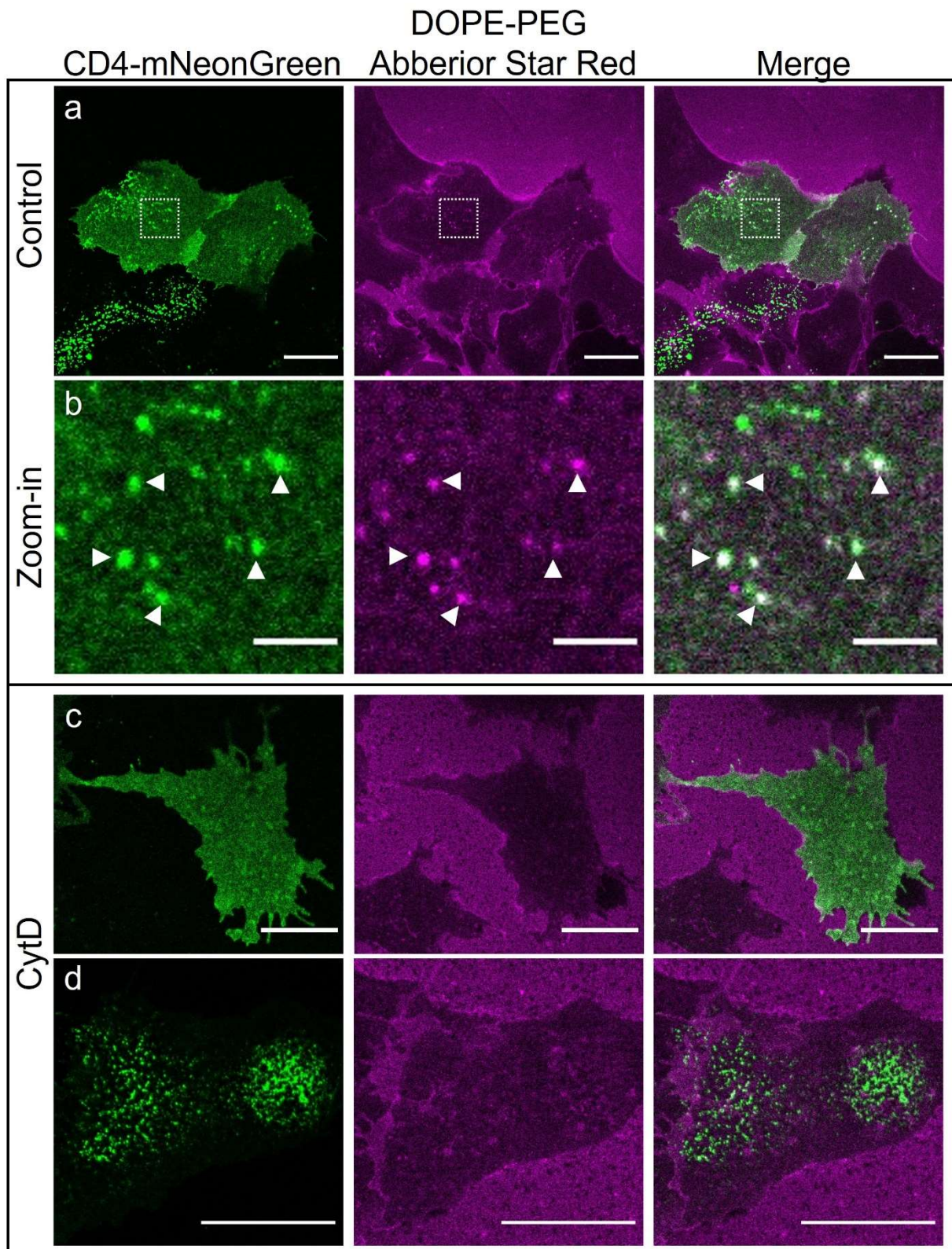


**Figure 9.** Membrane organisation of **CD4-mNeonGreen** in the basal plasma membrane of **U2OS** cells. Figure shows confocal images taken at the cover glass interface of **CD4-mNeonGreen** expressing **U2OS** cells, labelled with **DOPE-PEG-ASR**. **a** and **b** show untreated **U2OS** cells, with **(b)** clusters of **CD4-mNeonGreen** highlighted in the zoom-in. The clusters display co-localisation with **DOPE-PEG-ASR** (examples of colocalizing clusters indicated with white arrows in **b**). **c** and **d** show representative images of **CytD** treated **U2OS** cells. Upon **CytD** treatment, two cell populations were formed. **(c)** One population exhibited a similar membrane distribution of **CD4-SH4-mNG** as in untreated cells, despite having a changed overall cell morphology. **(d)** The other population had large ( $\sim 590 \text{ nm}^2$ ), heterogeneously distributed clusters spread along the membrane. Scale bar in **a**, **c** and **d** is  $20 \mu\text{m}$ . Scale bar in **b** is  $4 \mu\text{m}$ .

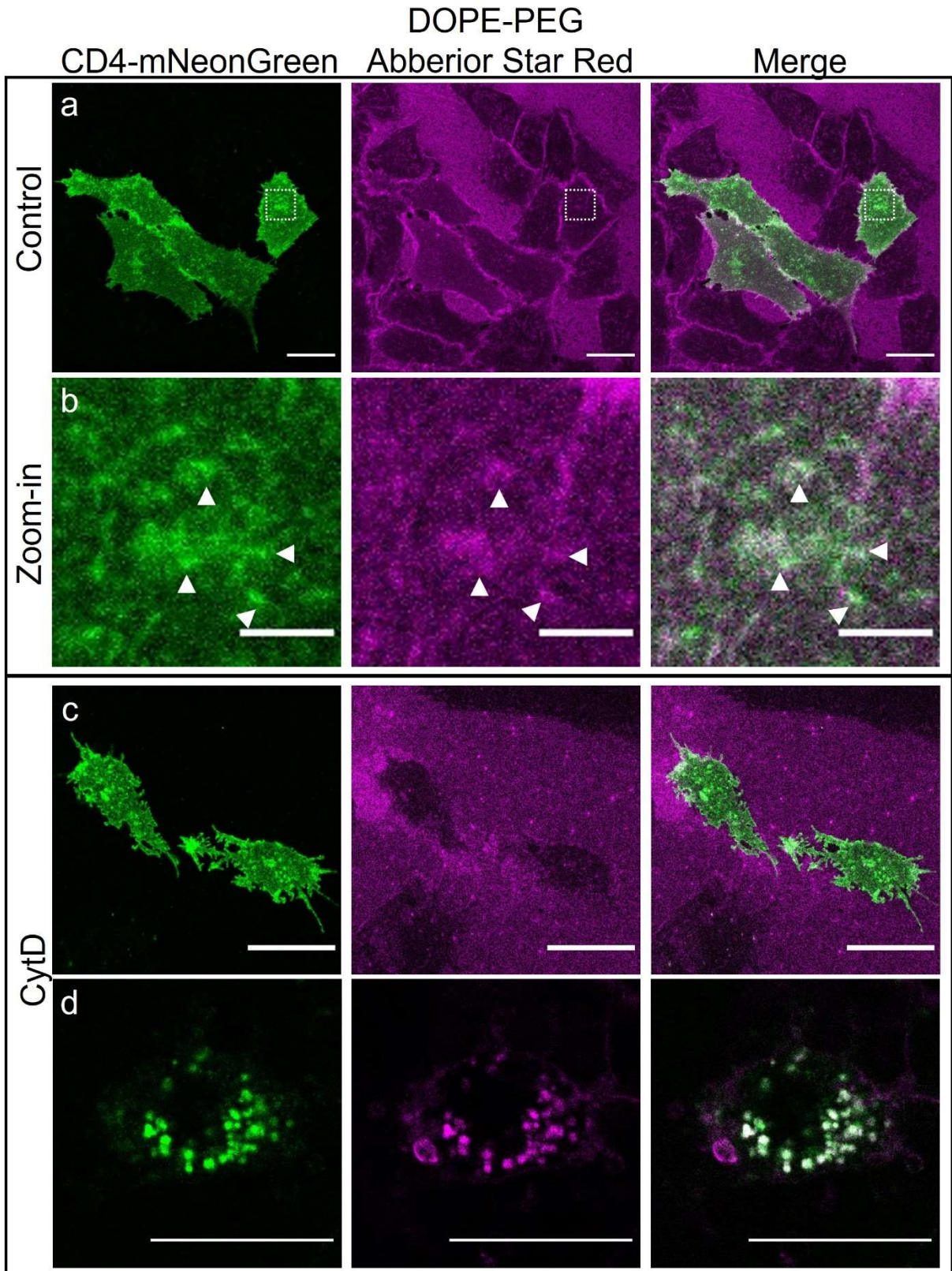


**Figure 10.** Membrane organisation of CD4-mNeonGreen in the basal plasma membrane of CHO cells. Figure shows confocal images taken at the cover glass interface of CD4-mNeonGreen expressing CHO cells, labelled with DOPE-PEG-ASR. **a** and **b** show untreated CHO cells, with **(b)** clusters of CD4-mNeonGreen highlighted in the zoom-in. The clusters display co-localisation with DOPE-PEG-ASR (examples of colocalizing clusters indicated with white arrows in **b**). **c** and **d** show representative images of CytD treated CHO cells. Upon CytD treatment, two cell populations were formed. **(c)** One population exhibited a similar membrane distribution of CD4-SH4-mNG as in untreated cells, despite having a changed overall cell morphology. **(d)** The other population had large (~1.09  $\mu\text{m}^2$ ), heterogeneously distributed clusters spread along the membrane. Scale bar in **a**, **c** and **d** is 20  $\mu\text{m}$ . Scale bar in **b** is 4  $\mu\text{m}$ .



populations were formed. One population, which represented the majority of cells, exhibited a similar Lck-SH4-mNG membrane distribution as in the control condition, despite having a changed overall cell morphology (figure 6C, figure 7C). The other, smaller population had larger (U2OS:  $\sim 700 \text{ nm}^2$ ; CHO:  $\sim 620 \text{ nm}^2$ ), heterogeneously distributed clusters spread along the membrane surface (figure 6D, figure 7D). In GPMVs, however, no Lck-SH4-mNG clusters were seen (figure S9A and figure S10A).

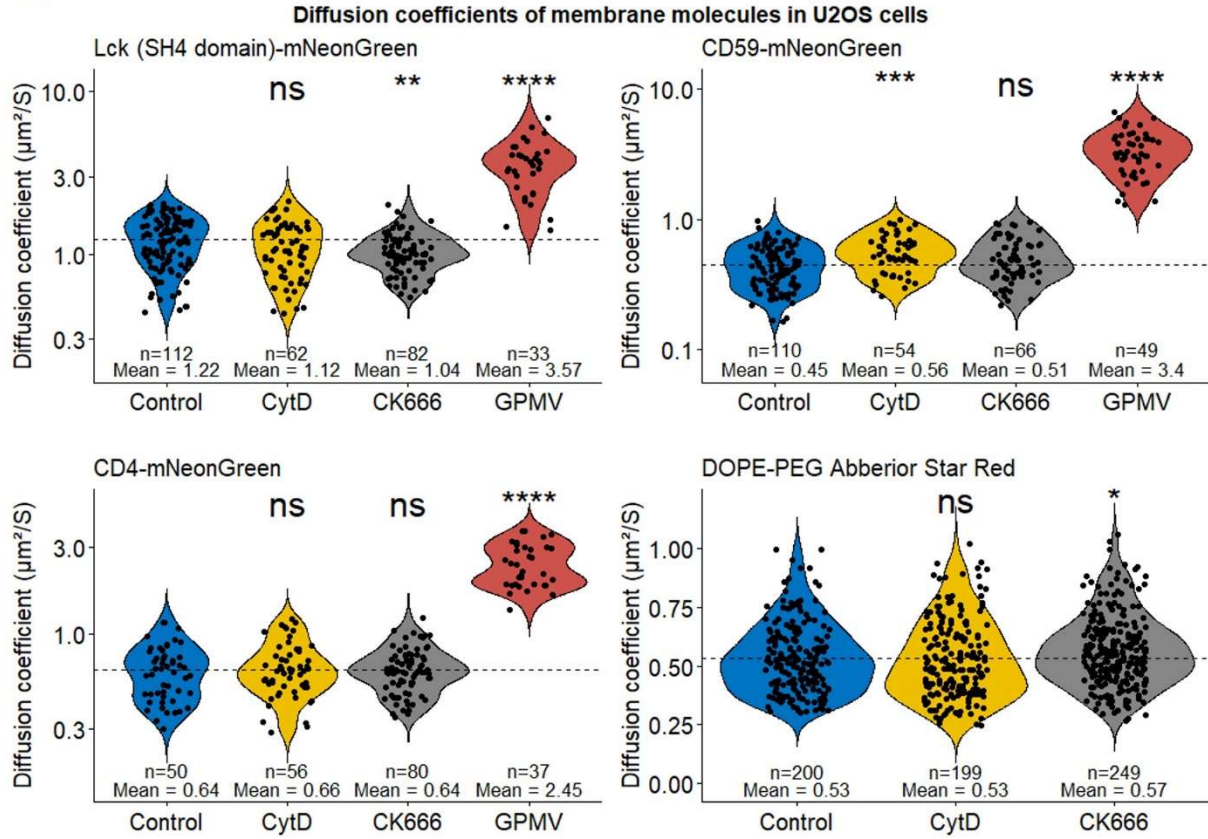
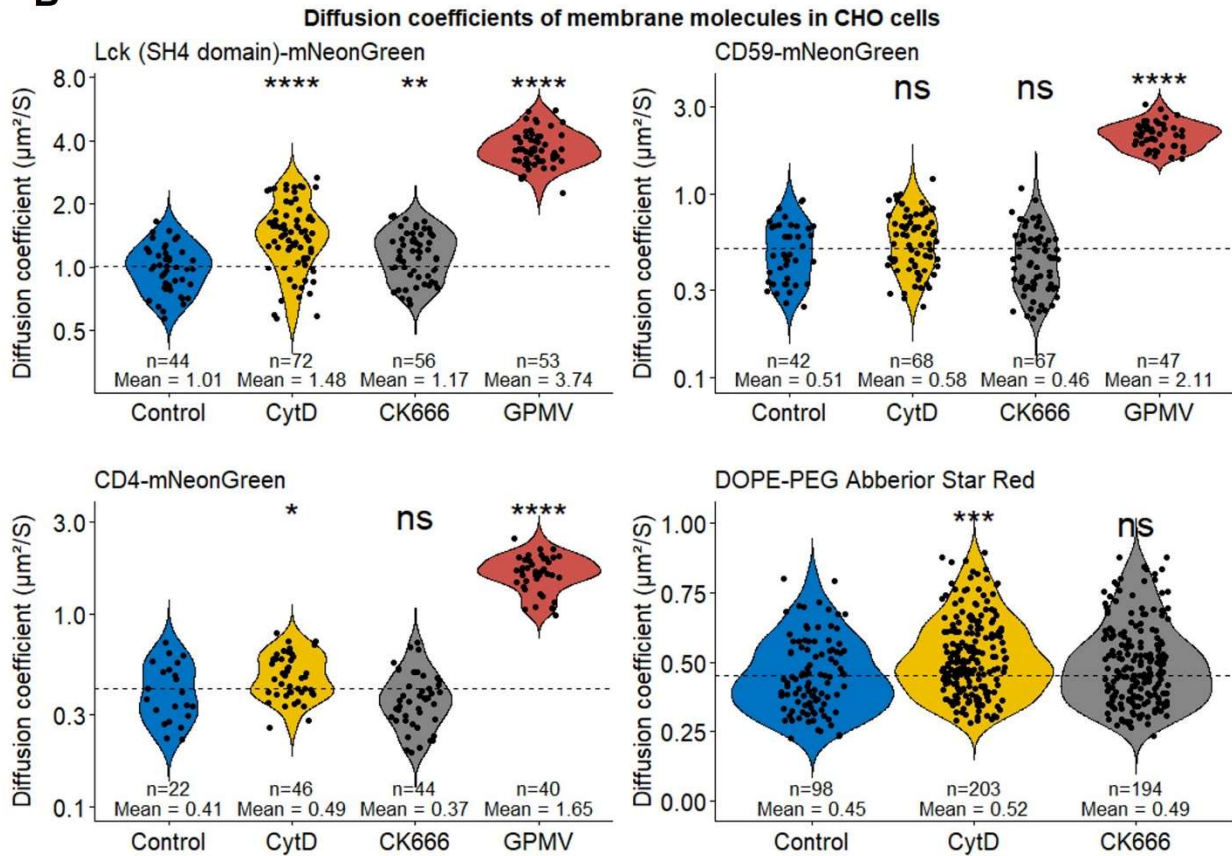
In accordance with the work of Schneider et al., the GPI-AP CD59 displayed membrane clusters in U2OS and CHO cells (figure 8) (2). No significant difference was found in cluster size between the two cell lines (U2OS:  $440 \text{ nm}^2$  average size; CHO:  $490 \text{ nm}^2$  average size;  $p = 0.44$ ). Additionally, they did not show changes in size or quantity upon either CK666 or CytD treatment (figure S3 and figure S6). These clusters were found to colocalize with DOPE-PEG-ASR (U2OS:  $r = 0.25$ ; CHO:  $r = 0.47$ ; figure 8Ab and figure 8Bb). In GPMVs, CD59-mNG was homogeneously distributed along the membranes, without visible clusters (figure S9B and figure S10B).

CD4-mNG had a similar membrane organisation as Lck-SH4-mNG. In both cell lines, CD4-mNG formed bright clusters which somewhat colocalised with DOPE-PEG-ASR when untreated or treated with CK666 (U2OS:  $r = 0.24$ ; CHO:  $r = 0.26$ , figure 9A-B, figure 10A-B). In U2OS cells, these clusters had an average size of  $370 \text{ nm}^2$ . However, in CHO cells, they were significantly smaller, with an average size of  $278 \text{ nm}^2$  ( $p = 0.03$ ). Similarly to Lck-SH4-mNG, two cell populations were formed upon CytD treatment. One population exhibited a similar organisation of CD4-mNG as with cells in the control condition, despite having an overall changed cell morphology (figure 9C, figure 10C). The other population displayed large clusters (U2OS:  $\sim 590 \text{ nm}^2$ ; CHO:  $\sim 1.09 \mu\text{m}^2$ ) of CD4-mNG (figure 9D, figure 10D). No clusters were visible in GPMVs, however (figure S9C, figure S10C).

Overall, the results presented here indicate Lck-SH4-mNG, CD4-mNG and CD59 to form membrane clusters. Additionally, CytD-treatment results in an intensified membrane clustering of Lck-SH4-mNG and CD4-mNG, but has no visible effect on the membrane clustering of CD59-mNG. This clustering was not seen for any of the proteins in GPMVs, however.

#### *The actin cytoskeleton affects membrane diffusion differently between cell lines*

To study the effects of the cortical actin cytoskeleton, we measured membrane molecule mobility with FCS. CHO and U2OS cells expressing Lck-SH4-mNG, CD59-mNG, or CD4-mNG were labelled with DOPE-PEG-ASR and treated with either CytD or CK666 (figure 2).

**A****B***Figure legend on next page.*

**Figure 11.** The diffusion coefficients of Lck-mNG, CD59-mNG, CD4-mNG and DOPE-PEG-ASR in live U2OS and CHO cells, and cell-derived GPMVs as determined by FCS. **(A)** Diffusion coefficients of Lck-mNG (top-left), CD59-mNG (top-right), CD4-mNG (bottom-left) and DOPE-PEG-ASR (bottom-right) in live U2OS cells treated with CytD, CK666 and in U2OS-derived GPMVs. **(B)** Diffusion coefficients of Lck-mNG (top-left), CD59-mNG (top-right), CD4-mNG (bottom-left) and DOPE-PEG-ASR (bottom-right) in live CHO cells treated with CytD, CK666 and in CHO-derived GPMVs. **A** and **B** display substantial cell-dependent differences in diffusion coefficients in live U2OS and CHO cells. Additionally, the diffusion of all measured proteins are substantially faster in GPMVs than in the live cells. *n* represents the number of diffusion coefficients, determined from individual measurements. Mean represents the mean diffusion coefficient per condition. ns:  $p > 0.05$ , \*:  $p \leq 0.05$ , \*\*:  $p \leq 0.01$ , \*\*\*:  $p \leq 0.001$ , \*\*\*\*:  $p \leq 0.0001$

---

Additionally, to test the effects of a complete absence of the actin cytoskeleton on membrane protein diffusion, measurements were performed on GPMVs that were isolated from identical cells.

In U2OS cells, treatment with CytD or CK666 did not induce major changes in the determined *D* values (figure 11A, figure S11A). Statistically significant differences from the control were found for Lck-SH4-mNG (fold-change = 0.85,  $p = 0.005$ ) and DOPE-PEG-ASR (fold-change = 1.06,  $p = 0.042$ ) after CK666 treatment, and CD59-mNG (fold-change = 1.25,  $p = 0.001$ ) after CytD treatment. However, a substantial spread was present in the dataset. This, as well as the relatively minor (fold-)changes in *D*, may cause the biological significance of the effects of CytD and CK666 on membrane protein and lipid diffusion in U2OS cells to be challenged. In contrast, diffusion of Lck-SH4-mNG, CD59-mNG and CD4-mNG was substantially faster in GPMVs. For Lck-SH4-mNG, the diffusion was approximately 2.9 times faster ( $p < 0.0001$ ), for CD4-mNG approximately 3.9 times faster ( $p < 0.0001$ ) and for CD59-mNG approximately 7.6 times faster ( $p < 0.0001$ ) (figure S11).

In untreated CHO cells, diffusion of Lck-SH4-mNG, CD4-mNG and DOPE-PEG-ASR was slower than in untreated U2OS cells ( $p \leq 0.002$ ) (figure 11). Compared to the control, Lck-SH4-mNG exhibited faster diffusion after treatment with CytD (fold-change = 1.46,  $p = 0.001$ ) and CK666 (fold-change = 1.16,  $p = 0.006$ ) (figure 11B, figure S11B). CytD treatment further led to slight increases of *D* of CD4-mNG (fold-change = 1.19,  $p = 0.04$ ) and DOPE-PEG-ASR (fold-change = 1.15,  $p = 0.0007$ ). These results suggest the actin cytoskeleton to have the largest effect on the membrane mobility of Lck-SH4-mNG, as both actin cytoskeleton-disrupting drugs induced faster diffusion of this protein, rather than only one of the used drugs. The diffusion of membrane proteins was much faster in GPMVs than in live cells. In CHO-derived GPMVs, Lck-SH4-mNG displayed 3.7 times faster diffusion ( $p < 0.0001$ ), CD59-mNG showed 4.2 times faster diffusion ( $p < 0.0001$ ) and CD4-mNG showed 4 times faster diffusion ( $p < 0.0001$ ) than in untreated CHO cells (figure S11).

In total, the much faster diffusion of membrane proteins in GPMVs highlight the importance of the actin cytoskeleton to membrane diffusion. Furthermore, these results also indicate there

to be cell-dependent variations in diffusion coefficients. This may be due to differences of the cortical actin mesh densities and membrane compartment sizes, which would explain the CHO-specific increase in diffusion coefficient of Lck-SH4-mNG upon CytD and CK666 treatment.

*Changes in diffusion coefficient are not necessarily linked with changes of the anomalous factor*

Not only does confocal FCS enable determining the average diffusion coefficient of fluorescent molecules, it also provides information on the diffusion mode. Through FCS curve fitting, the anomalous factor  $\alpha$  can be determined (see “Data analyses” under methods section for details). When  $\alpha$  is different from 1, the molecule is said to undergo anomalous diffusion, rather than free Brownian motion. If  $\alpha < 1$ , the molecule undergoes subdiffusion (e.g. due to membrane compartmentalisation or lipid raft incorporation). In contrast, if  $\alpha > 1$ , the molecule undergoes superdiffusion (e.g. due to active cellular transport processes) (34).

In untreated U2OS cells,  $\alpha$  was significantly different from 1 for Lck-SH4-mNG (mean  $\alpha = 0.87$ ,  $p < 0.0001$ ), CD59-mNG (mean  $\alpha = 0.97$ ,  $p = 0.032$ ) and DOPE-PEG-ASR (mean  $\alpha = 1.06$ ,  $p < 0.0001$ ) (figure 12A). However, for CD59-mNG and DOPE-PEG-ASR, the biological significance of these minor alterations from 1 might be debatable. Nevertheless, these results suggest a relatively substantial hindrance in the diffusion of Lck-SH4-mNG in U2OS cells. Additionally, upon treatment of U2OS cells with CK666, the mean  $\alpha$  exhibits a significant increase for Lck-SH4-mNG, from 0.87 to 0.92 ( $p = 0.0008$ ). For CD59-mNG, the mean  $\alpha$  increased from 0.97 to 1.02 upon CK666 treatment ( $p = 0.04$ ), but decreased with approximately 8% to 0.89 in GPMVs ( $p = 0.0009$ ). In contradiction to the hypothesis, this suggests an increased hindrance to diffusion in GPMVs, relative to live cells.

Similar to their behaviour in U2OS cells, Lck-SH4-mNG and DOPE-PEG-ASR show anomalous diffusion in untreated CHO cells (Lck-SH4-mNG:  $\alpha = 0.92$ ,  $p < 0.0001$ ; DOPE-PEG-ASR:  $\alpha = 1.11$ ,  $p < 0.0001$ ) (figure 12B). However, in contrast to what was determined in U2OS cells, CD59-mNG did not show anomalous diffusion, but CD4-mNG did ( $\alpha = 0.87$ ,  $p < 0.0001$ ). Interestingly, despite the substantially faster diffusion of Lck-SH4-mNG upon CytD treatment and GPMV formation, these treatments induced a statistically significant decrease of the mean  $\alpha$ . Both these conditions led to a decrease of approximately 7% (CytD:  $\alpha = 0.86$ ,  $p = 0.006$ ; GPMV:  $\alpha = 0.86$ ,  $p = 0.005$ ). However, the biggest change in diffusion anomaly was seen for CD4-mNG. Despite having undergone no significant, or only minor increases of  $D$  upon CK666 or CytD treatment, respectively,  $\alpha$  increased significantly from 0.87 in response to both treatments (CytD:  $\alpha = 1.04$ ,  $p = 0.0001$ ; CK666:  $\alpha = 1.02$ ,  $p = 0.004$ ). Additionally, the

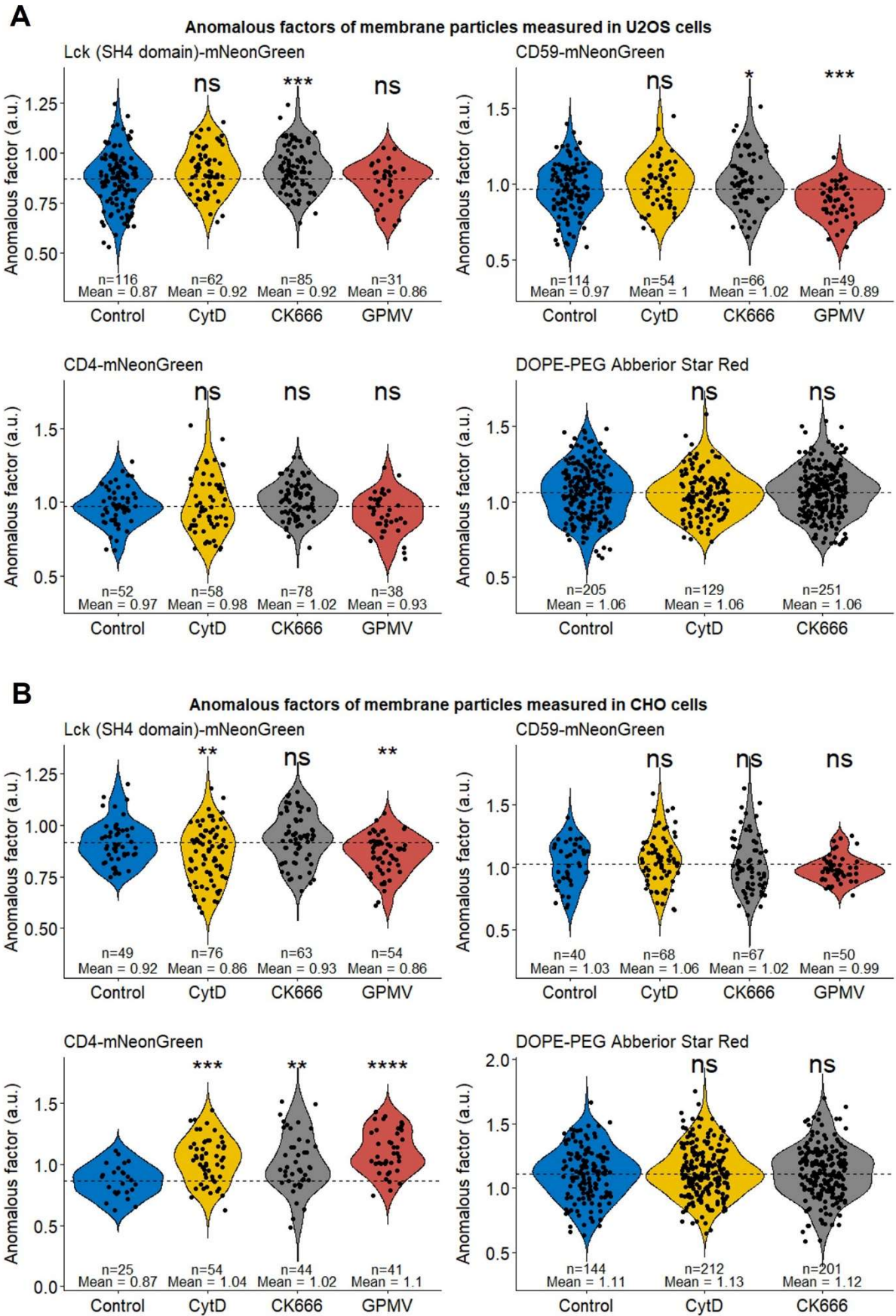


Figure legend on next page.

**Figure 12.** Anomalous factors of Lck-mNG, CD59-mNG, CD4-mNG and DOPE-PEG-ASR in U2OS and CHO cells and cell-derived GPMVs, as determined by FCS. **(A)** Anomalous exponents of Lck-mNG (top-left), CD59-mNG (top-right), CD4-mNG (bottom-left) and DOPE-PEG-ASR (bottom-right) in live U2OS cells treated with CytD, CK666 and in U2OS-derived GPMVs. **(B)** Anomalous factors of Lck-mNG (top-left), CD59-mNG (top-right), CD4-mNG (bottom-left) and DOPE-PEG-ASR (bottom-right) in live CHO cells treated with CytD, CK666 and in CHO-derived GPMVs. The results shown in **A** and **B** show there to be little correlation between changes in diffusion coefficients and changes in anomalous factors.  $n$  represents the number of diffusion coefficients, determined from individual measurements. Mean represents the mean anomalous factor per condition. ns:  $p > 0.05$ , \*:  $p \leq 0.05$ , \*\*:  $p \leq 0.01$ , \*\*\*:  $p \leq 0.001$ , \*\*\*\*:  $p \leq 0.0001$ .

---

large increase of  $D$  for CD4-mNG in GPMVs is paired with a substantial increase ( $\sim 26\%$ ) of  $\alpha$  ( $\alpha = 1.1$ ,  $p < 0.0001$ ). These results suggest an important role of the actin cytoskeleton towards the diffusion behaviour of CD4-mNG.

In total, the overall changes in  $\alpha$  measured in membrane molecules upon actin cytoskeletal disruption are cell-dependent, albeit minor. Interestingly, they also seem to display little correlation with changes of diffusion coefficients.

## DISCUSSION

This study aimed to elucidate the role of the actin cytoskeleton on the diffusion of inner leaflet-associated proteins, transmembrane proteins and GPI-APs. Using FCS, we have found the diffusion of Lck, CD4 and CD59 to be substantially faster in GPMVs. Additionally, Lck displayed faster diffusion in live CHO cells treated with either CytD or CK666. Such changes were not shown for CD59 and CD4 in this cell line, however. Interestingly, none of the proteins displayed substantial changes in diffusion coefficient in live U2OS cells (albeit some differences were statistically significant). These results provide three noteworthy points of discussion. First, the effects of the actin cytoskeleton-targeting drugs were shown to be cell-specific. Second, the results presented here suggest the actin cytoskeleton-targeting drugs to mainly manifest their effect on inner leaflet-associated proteins. Third, the much faster diffusion of all membrane proteins in GPMVs suggest a great increase in plasma membrane fluidity when there is a complete lack of actin cytoskeletal structures.

**The effects of actin-targeting drugs are cell-specific.** Numerous explanations could be given for the cell-dependent differences in diffusion coefficients. For example, differences in membrane viscosity or molecular crowding may explain the faster diffusion in untreated U2OS cells, compared to that in untreated CHO cells (35-37). However, if this were the case, CytD and CK666 would be expected to have similar effects on diffusion in both cell lines. This is not the case, however. Hence, a more suitable explanation may be a cell-dependent variance of the size of membrane compartments formed by cortical actin (figure 13A-B). Previous studies have

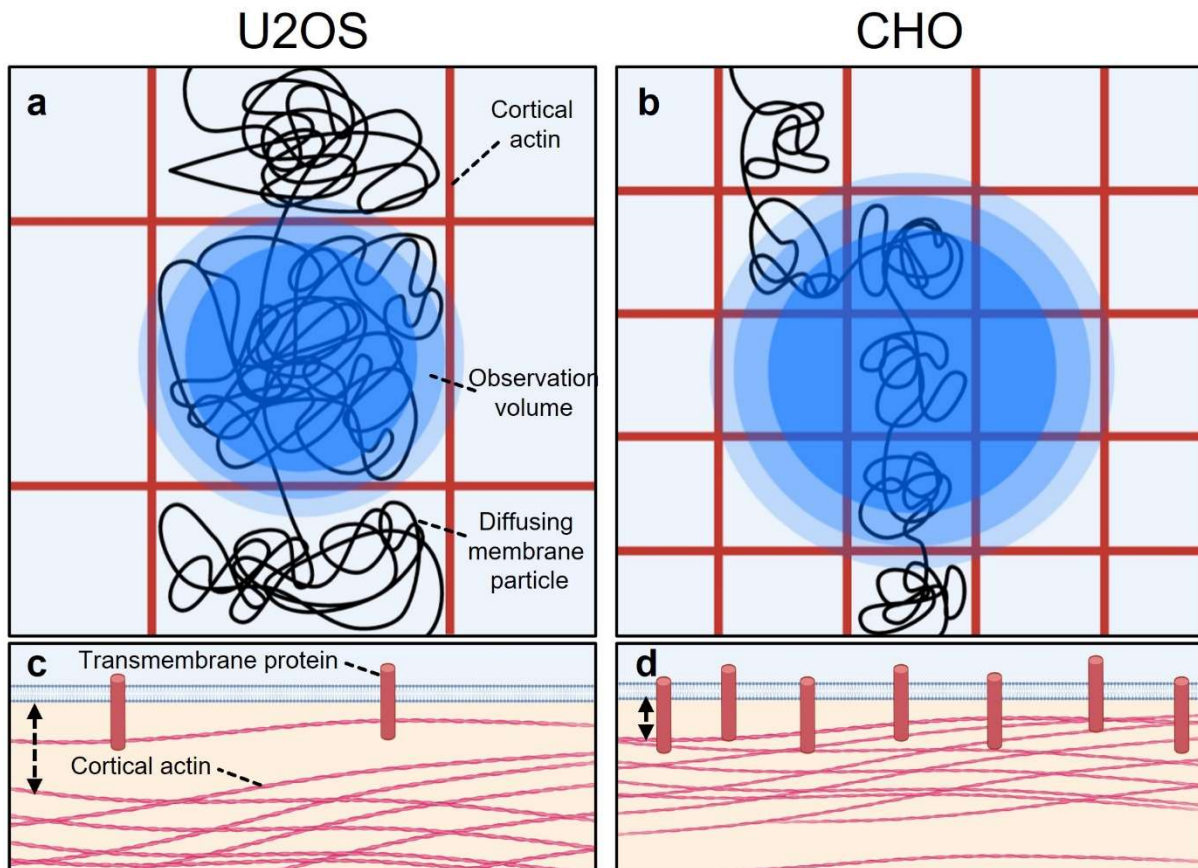


**Figure 13.** Schematic representation of cell-dependent differences in membrane compartmentalisation by the cortical actin cytoskeleton. **(a)** U2OS cells are hypothesised to contain larger membrane compartments than **(b)** CHO cells. This may be due to cell-dependent differences in membrane-cortex distance. High membrane-cortex distances will result in lower concentrations of actin at the plasma membrane and vice versa. **(c)** Therefore, high membrane-cortex distances will also lead to lower numbers of transmembrane proteins being immobilised by the cortical actin and larger membrane compartments. **(d)** Conversely, low membrane-cortex distances will lead to high numbers of transmembrane proteins being immobilised by the cortical actin, resulting in small membrane compartments. The dashed arrows in **c** and **d** indicate the membrane-cortex distance.

described cell lines to have differences in membrane-actin cortex distances, through differential expression of proteins of the ERM family. This results in variations in membrane tension and, therefore, cell morphology and cell migration (38, 39). Low membrane-cortex distances have also been shown to cause the cortical actin to have higher concentrations and to be less permeable at the plasma membrane (figure 13C-D). This would therefore strongly suggest there to be cell-dependent variations in membrane compartment size, resulting in cell-dependent diffusion dynamics (11, 38, 39). According to the picket-fence model, higher membrane compartmentalisation would lead to slower detected diffusion when measured at confocal resolutions. This would be due to the larger amount of “fences” that membrane molecules would need to “hop” within the focal volume. Conversely, if membrane compartments are larger than, or are approximately the same size as the microscope’s focal volume, membrane molecules will seem less restricted in their movement. Consequently, a faster diffusion will be detected at confocal resolutions (1-3, 17, 40-42). Additionally, it may be hypothesised that the

disruption of cortical actin (e.g. through the treatment with actin-targeting drugs) will have a lower relative impact on the cortical actin density within the observation volume when the initial actin density was low in untreated conditions. Therefore, CytD and CK666 treatment may be suggested to have a lower relative effect on the detected diffusion coefficients. The results presented in this work would be in line with this. Diffusion of Lck, CD4 and the unsaturated lipid analogue of DOPE was slower in untreated CHO cells, compared to in untreated U2OS cells. Additionally, none of the measured proteins displayed significantly faster diffusion in both CytD and CK666 treated U2OS cells, whereas this was the case for Lck in CHO cells. This explanation for the cell-dependent differences may further be corroborated by the clusters of Lck, CD4 and CD59 seen on the plasma membrane. First, these clusters were found to colocalise with DOPE. This lipid has previously been established to display hop diffusion and does not associate with lipid rafts (2, 40). Second, the membrane clusters of Lck and CD4 were significantly larger in U2OS cells than in CHO cells. As the membrane organisation of Lck and CD4 was greatly affected by CytD, it could be implied that the membrane organisation of these proteins is substantially affected by actin-dependent mechanisms. However, there remains a possibility that the membrane clustering of Lck, CD4 and CD59 may be the result of membrane ruffling or endocytic vesiculation. Hence, this is a topic that requires further investigation. To further explore this cell-dependency in membrane compartment size, continued studies in this field may benefit from using a wider range of cell lines. In some of the first works describing the picket-fence model, Normal Rat Kidney (NRK) epithelial cells were studied using single-molecule tracking to discover DOPE to be highly compartmentalised. However, upon treatment with Latrunculin A (a potent inhibitor of actin assembly), DOPE displayed a highly increased diffusion coefficient due to decreased hop-diffusion (40, 41). These results are in disagreement to the results shown in the present study. This therefore highlights the importance of using a wide range of cell lines to gain a full understanding of actin-dependent effects on membrane protein and lipid diffusion. In total, the data presented in this study suggests the cell-dependent differences in diffusion dynamics to be due to variations in size of the membrane compartments formed by cortical actin. However, this remains a topic of further experimental exploration.

Of additional interest, Clausen et al. have studied the density distribution of the actin cortex using super-resolution stimulated-emission-depletion (STED) microscopy. They established that cells can increase the adhesion energy between the cortical actin and the plasma membrane by over-activating ERM proteins at local and global scales (11, 43). Cells may thereby fine-tune membrane architecture by altering their lipid and protein distribution, aggregation and



diffusion dynamics (11). Hence, there might be variations in size of the actin-dependent membrane compartments along the lateral plane of the plasma membrane (11, 12). Although this is yet to be experimentally established, this may provide a viable explanation for the large spread of the diffusion data obtained within the same conditions of the present study (figure 11B-C).

**The actin cytoskeleton-targeting drugs mainly manifest their effect on inner leaflet-associated proteins.** As mentioned above, the results of the present study suggest the cortical actin to mainly manifest its effect on inner leaflet-anchored proteins. It may be assumed that, due to the cytosolic placement of the actin cytoskeleton, inner leaflet anchored proteins may experience higher steric hindrance by this structure. However, the picket-fence model proposed by Kusumi et al. states that the transmembrane proteins anchored to the cortical actin cytoskeleton (i.e. the “pickets”) cause the hindrance in diffusion, rather than the actin cytoskeleton itself. The transmembrane proteins not only impede diffusion through steric hindrance, but also increase the viscosity of the membrane around them. This causes the hydrodynamic friction to increase around these immobilised proteins, which therefore slows down the diffusion of the surrounding membrane molecules (42). Hence, it may be argued that inner leaflet-anchored proteins will experience steric hindrance by both the immobilised transmembrane proteins, as well as the cortical actin filaments. However, *in silico* studies have simulated the compartmentalising abilities of actin and have provided evidence that single filaments of actin provide little blockage to membrane proteins (44). This therefore provides insufficient explanation for the larger effect of actin cytoskeleton-dependent hindrance to inner leaflet-anchored protein diffusion. Thus, this remains a topic of interest and will require further experimental exploration.

**Membrane proteins exhibit faster diffusion in GPMVs.** The present study has shown substantial increases of the diffusion coefficients for Lck, CD4 and CD59 in GPMVs. This strongly suggests the cortical actin cytoskeleton to modulate membrane diffusion of all these proteins. However, these increases of diffusion coefficients were not seen for CD4 and CD59 in either live CHO or U2OS cells upon CytD and CK666 treatment. These results may thereby highlight the limitations of this cell-derived membrane model. One of the obvious pitfalls of GPMVs are the covalent modifications caused by the vesiculation agents. For example, it is well established that DTT induces protein depalmitoylation (45). Therefore, palmitoylated proteins such as Lck and CD4 may exhibit membrane organisations in GPMVs that differ greatly from their endogenous counterparts (as is shown in figure 6, 7, 9, 10, S9 and S10). For example, CD4’s lipid raft association depends on its palmitoylation sites. Hence, DTT-

dependent depalmitoylation may prevent CD4 from associating with lipid rafts in GPMVs. Additionally, the depalmitoylation induces plasma membrane dissociation of Lck and CD4 (figure S10A+C). Therefore, autocorrelation curves obtained from diffusion measurements in GPMV membranes may show a second, faster diffusing component, which represents luminal protein diffusion. These undesirable effects may be circumvented with adapted GPMV isolation protocols, which use NEM as the vesiculation agent. However, the present study has shown that not all cell lines (e.g. CHO cells) are compatible with this protocol (figure S1). Furthermore, the plethora of cellular events that lead to GPMV isolation result in various membrane modifications that may drastically alter the diffusion dynamics of all membrane proteins. For example, many GPI-APs, including CD59, have been suggested to localise to and to stabilise lipid rafts in clusters of approximately six receptor molecules (42, 46, 47). These clusters undergo slow, Brownian diffusion and transiently recruit lipid raft-associated lipids, such as GM1 and GM3 (48, 49). Additionally, larger CD59 clusters rich in lipid raft-associated lipids have been suggested to interact with the actin cytoskeleton through an as of yet unidentified transmembrane protein (42, 50, 51). However, GPMV isolation leads to a great re-organisation of the lipids within the plasma membrane. Namely, a loss of membrane leaflet asymmetry, typically defined by the exposure of PS, is seen (2, 7). Although the extent of this loss of membrane asymmetry is currently not known, its effect on membrane organisation and composition is far from negligible (7, 52). Therefore, it is likely that proteins with a mobility that is strongly connected to the organisation of the plasma membrane, such as CD4 and CD59, will display altered diffusion characteristics in GPMVs, for reasons other than the absence of the cortical actin cytoskeleton. Furthermore, GPMVs represent the cellular plasma membrane in a state of thermodynamic equilibrium. In contrast, live cell membranes are highly dynamic and out-of-equilibrium structures (7). The numerous limitations discussed in this section may result in drastically altered membrane organisations and mobility for proteins such as Lck, CD59 and CD4. Hence, although there is a consensus that membrane dynamics are mostly affected by the absence of an intact actin cortex, the altered membrane composition of GPMVs likely affects diffusion dynamics in not-insignificant manners (2). However, despite these limitations, GPMVs still provide crucial information on the role of the actin cytoskeleton in membrane diffusion dynamics. Therefore, when applied in combination with additional experimental models (e.g. drug treatments in live cells), GPMVs remain a valuable system in studies regarding the actin-dependency of membrane diffusion dynamics.

## OUTLOOK

Lck, CD59 and CD4 each represent a class of proteins with different membrane placement and distribution. However, these classes each consist of hundreds, if not thousands of proteins with unique functions, membrane distributions and diffusion characteristics. For example, GPI-APs range in size from only 12 amino acids (i.e. CD52) to more than 200 kDa (i.e. alpha-tectorin). Furthermore, they include a wide variety in functions, including enzymes, receptors, adhesion molecules, protease inhibitors, complement regulators and prions (19). Therefore, the formation of a “one-size-fits-all” model for membrane diffusion characteristics would most likely be impossible, even for proteins with identical membrane placement mechanisms. Moreover, proteins are incorporated into the plasma membrane through a much wider variety of mechanisms than those investigated in the present study. For example, CD4 is a monomeric type I transmembrane glycoprotein, with only one transmembrane domain consisting of an amphipathic  $\alpha$ -helix (53-55). Nevertheless, numerous proteins contain multiple transmembrane domains, consisting of either  $\alpha$ -helices or  $\beta$ -sheets. For example, the wide class of G-protein coupled receptors all consist of seven  $\alpha$ -helical transmembrane domains (53). Further, a large class of proteins incorporates itself into the inner leaflet of the plasma membrane through fission of an amphipathic  $\alpha$ -helix, without lipid anchor as is the case for Lck (53, 56). Hence, future studies will need to apply a much wider variety of protein markers to acquire a full understanding of the actin-dependent membrane compartmentalisation of proteins.

In the present study, confocal FCS has provided a wealth of information regarding the diffusion of membrane proteins. However, a number of conflicting results may cast doubts on the value of this technique when studying the anomaly of membrane molecule diffusion. First, changes of the anomalous factor obtained through autocorrelation curve fitting displayed little correlation with changes in diffusion coefficients of membrane proteins. For example, Lck, CD4 and CD59 exhibited substantially faster diffusion in GPMVs (figure 11). However, for the majority of the measured proteins, the anomalous factor remained either unchanged or even decreased (figure 12). Furthermore, despite a lack of substantial change of the diffusion coefficient of CD4 in live CHO cells, a large increase of the anomalous factor was seen in all conditions. As discussed above, it would be expected that the detected diffusion will be faster when the anomalous factor increases, presumably due to decreased compartmentalisation (1, 2). This suggests that the anomalous factor obtained through fitting of confocal FCS curves does not properly represent the actual diffusion dynamics of membrane molecules. Hence, it may be necessary to study the diffusion dynamics of proteins at not just confocal resolutions, but also at higher resolutions. When performing FCS measurements with conventional confocal

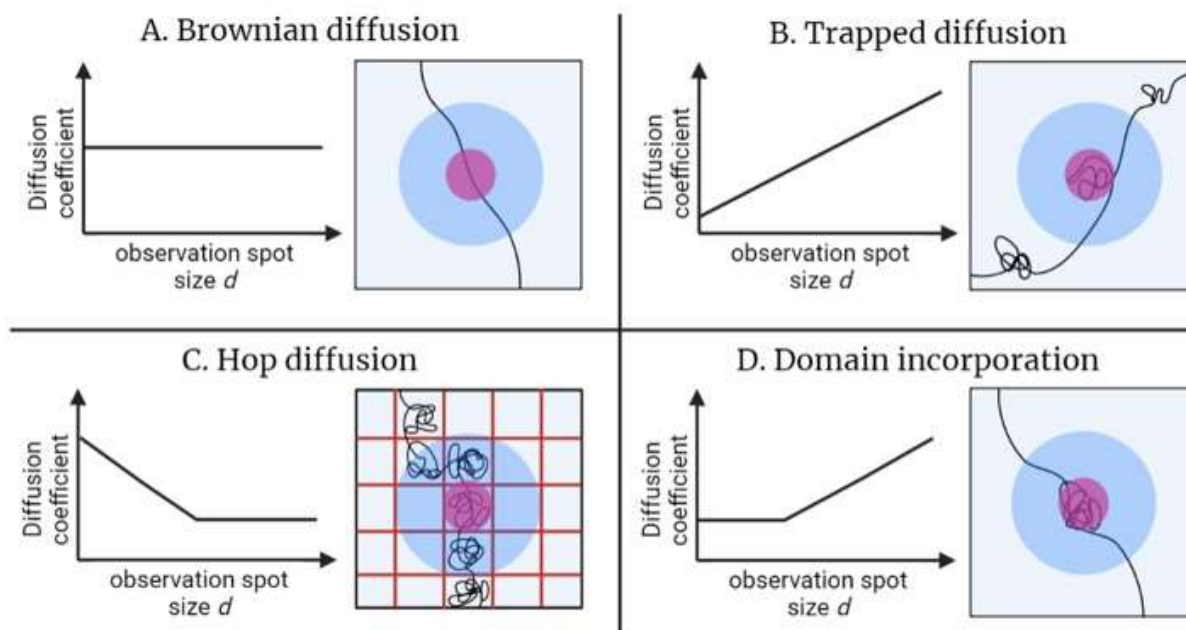


**Figure 14.** Schematic representation of the possible diffusion modes in the plasma membrane, **(left)** revealed by determining the diffusion coefficient at different observation spot sizes with STED-FCS and **(right)** the potential molecular mechanisms behind these diffusion modes (black: diffusion pathway of membrane molecule, light blue: confocal FCS observation spot, magenta: STED-FCS observation spot, red: cortical actin). **(A)** Free Brownian motion, in which the diffusion coefficient will not change with varying observation spot sizes. **(B)** Trapped diffusion, in which a membrane molecule becomes transiently immobilised through the binding to immobile or slow-moving interaction partners. The diffusion coefficient drops with decreasing spot size. **(C)** Hop diffusion, in which membrane molecules are compartmentalised by e.g. the cortical actin network and its associated network of transmembrane proteins. This leads to a fast diffusion within the compartment, with a high diffusion coefficient at low observation spot sizes. However, at observation spot sizes larger than the area of confinement, the diffusion coefficient will decrease. **(D)** Domain incorporation, in which the membrane molecule is incorporated into a domain, such as a lipid raft. Here, the diffusion coefficient remains constant when measured at observation spots of similar sizes as the domain. However, the diffusion coefficient increases with growing observation spot sizes when its diameter is above the size of the domain. Adapted from Schneider et al. (2).

microscopy, the minimal observation spot size is limited by the diffraction limit to approximately 200 nm. However, STED-FCS enables a reduction of the minimal observation spot size down to below 40 nm. This therefore facilitates diffusion measurements closer to the length scales of the features that cause constraints in membrane molecule diffusion (1-3, 18). Furthermore, when measuring the diffusion of membrane molecules at varying observation spot sizes – as is the case for STED-FCS – it is also possible to determine the diffusion mode (2, 3, 18, 57). There are numerous possible diffusion modes that each define how the detected  $D$  of a membrane molecule will change with varying observation spot size. In the case of a molecule undergoing free Brownian motion, the  $D$  will not change with varying observation spot sizes (figure 14A). However, in the case of trapped diffusion – in which a membrane molecule becomes transiently immobilised through the binding to immobile or slow-moving interaction partners –  $D$  drops with decreasing spot size (figure 14B). In hop diffusion, membrane molecules may be compartmentalised by e.g. the cortical actin network and its associated

network of transmembrane proteins. This leads to a fast diffusion within the compartment, with  $D$  increasing with a lower observation spot size. However, at observation spot sizes larger than the area of confinement,  $D$  will be smaller (figure 14C). Lastly, in the case of domain incorporation, in which the membrane molecule is incorporated into a domain, such as a lipid raft. Here,  $D$  remains constant when measured at observation spots of similar sizes as the domain. However, as with trapped diffusion,  $D$  increases with growing observation spot sizes when its diameter is above the size of the domain (figure 14D). The diffusion modes of membrane molecules are strongly dependent on their bioactivity and interaction dynamics (2, 3, 18). Hence, this STED-FCS can provide substantially more information regarding the diffusion dynamics and bioactivity of membrane molecules than confocal FCS. Therefore, further studies using STED-FCS may acquire more detailed information on the effects of CytD and CK666 on the diffusion of Lck, CD4 and CD59 in live cells. Furthermore, STED-FCS may also enable characterisation of the cell-dependent differences in membrane compartment sizes and their effect on membrane molecule diffusion.

Improving our understanding of membrane diffusion dynamics will consequently lead to an increased understanding of human health and disease. For example, membrane heterogeneity has been linked to cancer, cardiovascular disease and various host-pathogen interactions (2, 3). Mattila et al. have proposed a system in which the actin cytoskeleton provides a dynamic mechanism to regulate immune signalling (10). Here, a cell can modify its receptor organisation and dynamics in response to environmental stimuli. In B cells, the actin cytoskeleton has been suggested to be modified upon Toll-like receptor activation. Subsequently, the organisation of the actin cytoskeleton is altered to disrupt the diffusion barriers of B cell receptor (BCR) proteins. The resulting increase in free Brownian diffusion makes it more likely for the BCR to encounter the CD19 co-receptor. Therefore, the modification of the actin cytoskeleton makes the BCR activation a more probable outcome (10). This example highlights the importance of the research conducted in this study. Continued research in this field using STED-FCS and a wider range of cell types and membrane proteins will lead to a further gain of our fundamental knowledge of plasma membrane diffusion. Consequently, our knowledge will be improved on topics such as autoimmune disorders, immune cell malignancies and may aid in the formation of effective vaccination strategies (10).

## CONCLUSION

To conclude, the present study has found the actin cytoskeleton to play a confining role in the diffusion of inner leaflet-anchored proteins, transmembrane proteins and GPI-APs using

cell-derived GPMVs. By applying actin cytoskeleton-disrupting drugs in live cells, this effect was shown to be largest for the inner leaflet anchored proteins. Most notable, however, are the strong cell-dependent effects of cortical actin on membrane protein diffusion. The results obtained in this study thereby highlight the importance and complexity of the cortical actin cytoskeleton in the modulation of membrane protein diffusion. Therefore, they will aid in our understanding of plasma membrane diffusion dynamics and may act as stepping stones for continued research in the field.

## REFERENCES

1. Andrade DM, Clausen MP, Keller J, Mueller V, Wu C, Bear JE, et al. Cortical actin networks induce spatio-temporal confinement of phospholipids in the plasma membrane – a minimally invasive investigation by STED-FCS. *Scientific Reports*. 2015;5(1):11454.
2. Schneider F, Waithe D, Clausen MP, Galiani S, Koller T, Ozhan G, et al. Diffusion of lipids and GPI-anchored proteins in actin-free plasma membrane vesicles measured by STED-FCS. *Molecular biology of the cell*. 2017;28(11):1507-18.
3. Sezgin E, Levental I, Mayor S, Eggeling C. The mystery of membrane organization: composition, regulation and roles of lipid rafts. *Nature reviews Molecular cell biology*. 2017;18(6):361-74.
4. Danielli JF, Davson H. A contribution to the theory of permeability of thin films. *Journal of Cellular and Comparative Physiology*. 1935;5(4):495-508.
5. Singer SJ, Nicolson GL. The fluid mosaic model of the structure of cell membranes. *Science (New York, NY)*. 1972;175(4023):720-31.
6. Fujimoto T, Parmryd I. Interleaflet Coupling, Pinning, and Leaflet Asymmetry—Major Players in Plasma Membrane Nanodomain Formation. *Frontiers in Cell and Developmental Biology*. 2017;4(155).
7. Sezgin E, Kaiser HJ, Baumgart T, Schwille P, Simons K, Levental I. Elucidating membrane structure and protein behavior using giant plasma membrane vesicles. *Nature protocols*. 2012;7(6):1042-51.
8. Sych T, Gurdap CO, Wedemann L, Sezgin E. How Does Liquid-Liquid Phase Separation in Model Membranes Reflect Cell Membrane Heterogeneity? *Membranes*. 2021;11(5):323.
9. Charras GT, Hu C-K, Coughlin M, Mitchison TJ. Reassembly of contractile actin cortex in cell blebs. *Journal of Cell Biology*. 2006;175(3):477-90.
10. Mattila PK, Batista FD, Treanor B. Dynamics of the actin cytoskeleton mediates receptor cross talk: An emerging concept in tuning receptor signaling. *The Journal of cell biology*. 2016;212(3):267-80.
11. Clausen MP, Colin-York H, Schneider F, Eggeling C, Fritzsche M. Dissecting the actin cortex density and membrane-cortex distance in living cells by super-resolution microscopy. *Journal of physics D: Applied physics*. 2017;50(6):064002.
12. Chugh P, Paluch EK. The actin cortex at a glance. *Journal of Cell Science*. 2018;131(14).
13. Raghupathy R, Anilkumar AA, Polley A, Singh PP, Yadav M, Johnson C, et al. Transbilayer lipid interactions mediate nanoclustering of lipid-anchored proteins. *Cell*. 2015;161(3):581-94.

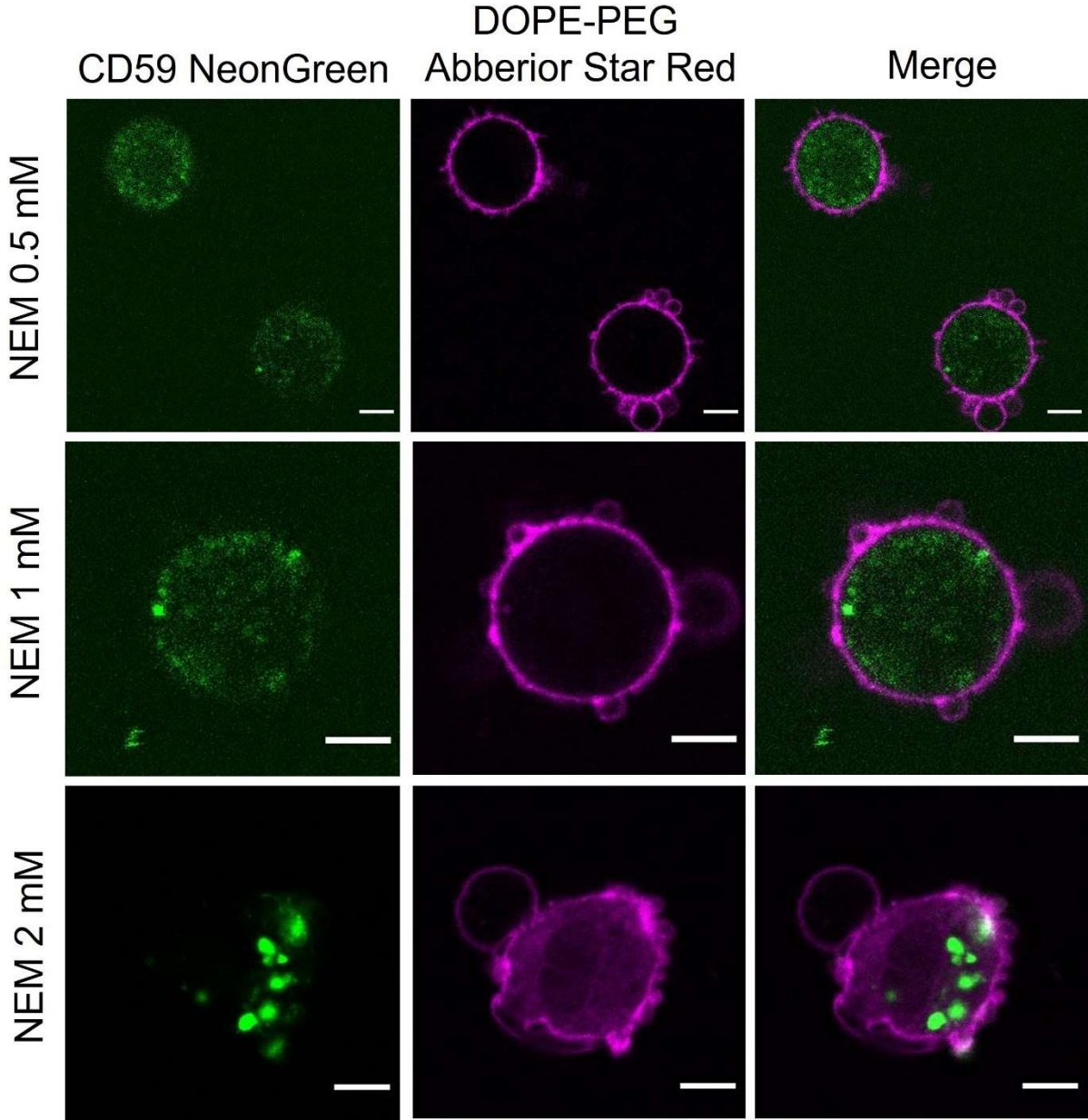
14. Fritzsche M, Li D, Colin-York H, Chang VT, Moeendarbary E, Felce JH, et al. Self-organizing actin patterns shape membrane architecture but not cell mechanics. *Nature Communications*. 2017;8(1):14347.
15. Elson EL. Fluorescence correlation spectroscopy: past, present, future. *Biophys J*. 2011;101(12):2855-70.
16. Kim SA, Heinze KG, Schwille P. Fluorescence correlation spectroscopy in living cells. *Nature methods*. 2007;4(11):963-73.
17. Sezgin E, Schneider F, Galiani S, Urbančič I, Waithe D, Lagerholm BC, et al. Measuring nanoscale diffusion dynamics in cellular membranes with super-resolution STED-FCS. *Nature protocols*. 2019;14(4):1054-83.
18. Sezgin E. Super-resolution optical microscopy for studying membrane structure and dynamics. *Journal of physics Condensed matter : an Institute of Physics journal*. 2017;29(27):273001.
19. Kinoshita T. Biosynthesis and biology of mammalian GPI-anchored proteins. *Open Biology*. 2020;10(3):190290.
20. Mobarak E, Javanainen M, Kulig W, Honigmann A, Sezgin E, Aho N, et al. How to minimize dye-induced perturbations while studying biomembrane structure and dynamics: PEG linkers as a rational alternative. *Biochimica et Biophysica Acta (BBA) - Biomembranes*. 2018;1860(11):2436-45.
21. Schneider CA, Rasband WS, Eliceiri KW. NIH Image to ImageJ: 25 years of image analysis. *Nature methods*. 2012;9(7):671-5.
22. Bolte S, Cordelières FP. A guided tour into subcellular colocalization analysis in light microscopy. *Journal of microscopy*. 2006;224(Pt 3):213-32.
23. Waithe D, Clausen MP, Sezgin E, Eggeling C. FoCuS-point: software for STED fluorescence correlation and time-gated single photon counting. *Bioinformatics (Oxford, England)*. 2016;32(6):958-60.
24. Sezgin E, Schwille P. Fluorescence techniques to study lipid dynamics. *Cold Spring Harbor perspectives in biology*. 2011;3(11):a009803-a.
25. Petrášek Z, Schwille P. Precise measurement of diffusion coefficients using scanning fluorescence correlation spectroscopy. *Biophys J*. 2008;94(4):1437-48.
26. Team RC. R: a language and environment for statistical computing. 2021.
27. Kassambara A. ggpubr: 'ggplot2' Based Publication Ready Plots. 2020.
28. Ayala YA, Pontes B, Hissa B, Monteiro ACM, Farina M, Moura-Neto V, et al. Effects of cytoskeletal drugs on actin cortex elasticity. *Experimental Cell Research*. 2017;351(2):173-81.
29. Cramer LP, Siebert M, Mitchison TJ. Identification of novel graded polarity actin filament bundles in locomoting heart fibroblasts: implications for the generation of motile force. *The Journal of cell biology*. 1997;136(6):1287-305.
30. Marcy Y, Prost J, Carlier M-F, Sykes C. Forces generated during actin-based propulsion: A direct measurement by micromanipulation. *Proceedings of the National Academy of Sciences of the United States of America*. 2004;101(16):5992-7.
31. Elkamhawy A, Ali E, Lee K. New horizons in drug discovery of lymphocyte-specific protein tyrosine kinase (Lck) inhibitors: a decade review (2011–2021) focussing on structure–activity relationship (SAR) and docking insights. *Journal of Enzyme Inhibition and Medicinal Chemistry*. 2021;36:1574-602.
32. Huang Y, Qiao F, Abagyan R, Hazard S, Tomlinson S. Defining the CD59-C9 Binding Interaction <sup>\*</sup>. *Journal of Biological Chemistry*. 2006;281(37):27398-404.
33. Mak TW, Saunders ME. 12 - The T Cell Receptor: Structure of Its Proteins and Genes. In: Mak TW, Saunders ME, editors. *The Immune Response*. Burlington: Academic Press; 2006. p. 311-40.

34. Banks DS, Fradin C. Anomalous Diffusion of Proteins Due to Molecular Crowding. *Biophys J*. 2005;89(5):2960-71.
35. Hill RJ, Wang C-Y. Diffusion in phospholipid bilayer membranes: dual-leaflet dynamics and the roles of tracer-leaflet and inter-leaflet coupling. *Proc Math Phys Eng Sci*. 2014;470(2167):20130843-.
36. Guigas G, Kalla C, Weiss M. Probing the nanoscale viscoelasticity of intracellular fluids in living cells. *Biophys J*. 2007;93(1):316-23.
37. Banks DS, Fradin C. Anomalous diffusion of proteins due to molecular crowding. *Biophys J*. 2005;89(5):2960-71.
38. Alert R, Casademunt J, Brugués J, Sens P. Model for Probing Membrane-Cortex Adhesion by Micropipette Aspiration and Fluctuation Spectroscopy. *Biophys J*. 2015;108(8):1878-86.
39. Liu Y, Belkina NV, Park C, Nambiar R, Loughhead SM, Patino-Lopez G, et al. Constitutively active ezrin increases membrane tension, slows migration, and impedes endothelial transmigration of lymphocytes in vivo in mice. *Blood*. 2012;119(2):445-53.
40. Fujiwara T, Ritchie K, Murakoshi H, Jacobson K, Kusumi A. Phospholipids undergo hop diffusion in compartmentalized cell membrane. *Journal of Cell Biology*. 2002;157(6):1071-82.
41. Kusumi A, Nakada C, Ritchie K, Murase K, Suzuki K, Murakoshi H, et al. Paradigm shift of the plasma membrane concept from the two-dimensional continuum fluid to the partitioned fluid: high-speed single-molecule tracking of membrane molecules. *Annual review of biophysics and biomolecular structure*. 2005;34:351-78.
42. Kusumi A, Suzuki KGN, Kasai RS, Ritchie K, Fujiwara TK. Hierarchical mesoscale domain organization of the plasma membrane. *Trends in Biochemical Sciences*. 2011;36(11):604-15.
43. Joanny JF, Kruse K, Prost J, Ramaswamy S. The actin cortex as an active wetting layer. *The European physical journal E, Soft matter*. 2013;36(5):52.
44. Lee KI, Im W, Pastor RW. Langevin dynamics simulations of charged model phosphatidylinositol lipids in the presence of diffusion barriers: toward an atomic level understanding of corralling of PIP2 by protein fences in biological membranes. *BMC Biophysics*. 2014;7(1):13.
45. Levental I, Grzybek M, Simons K. Raft domains of variable properties and compositions in plasma membrane vesicles. *Proceedings of the National Academy of Sciences*. 2011;108(28):11411-6.
46. Suzuki KGN, Fujiwara TK, Sanematsu F, Iino R, Edidin M, Kusumi A. GPI-anchored receptor clusters transiently recruit Lyn and G alpha for temporary cluster immobilization and Lyn activation: single-molecule tracking study 1. *The Journal of cell biology*. 2007;177(4):717-30.
47. Suzuki KG, Fujiwara TK, Edidin M, Kusumi A. Dynamic recruitment of phospholipase C gamma at transiently immobilized GPI-anchored receptor clusters induces IP3-Ca2+ signaling: single-molecule tracking study 2. *The Journal of cell biology*. 2007;177(4):731-42.
48. Suzuki KGN, Ando H, Komura N, Fujiwara T, Kiso M, Kusumi A. Unraveling of Lipid Raft Organization in Cell Plasma Membranes by Single-Molecule Imaging of Ganglioside Probes. In: Yamaguchi Y, Kato K, editors. *Glycobiophysics*. Singapore: Springer Singapore; 2018. p. 41-58.
49. Suzuki KGN. Lipid rafts generate digital-like signal transduction in cell plasma membranes. *Biotechnology Journal*. 2012;7(6):753-61.
50. Karbani N, Eshed-Eisenbach Y, Tabib A, Hoizman H, Morgan BP, Schueler-Furman O, et al. Molecular pathogenesis of human CD59 deficiency. *Neurology Genetics*. 2018;4(6):e280.

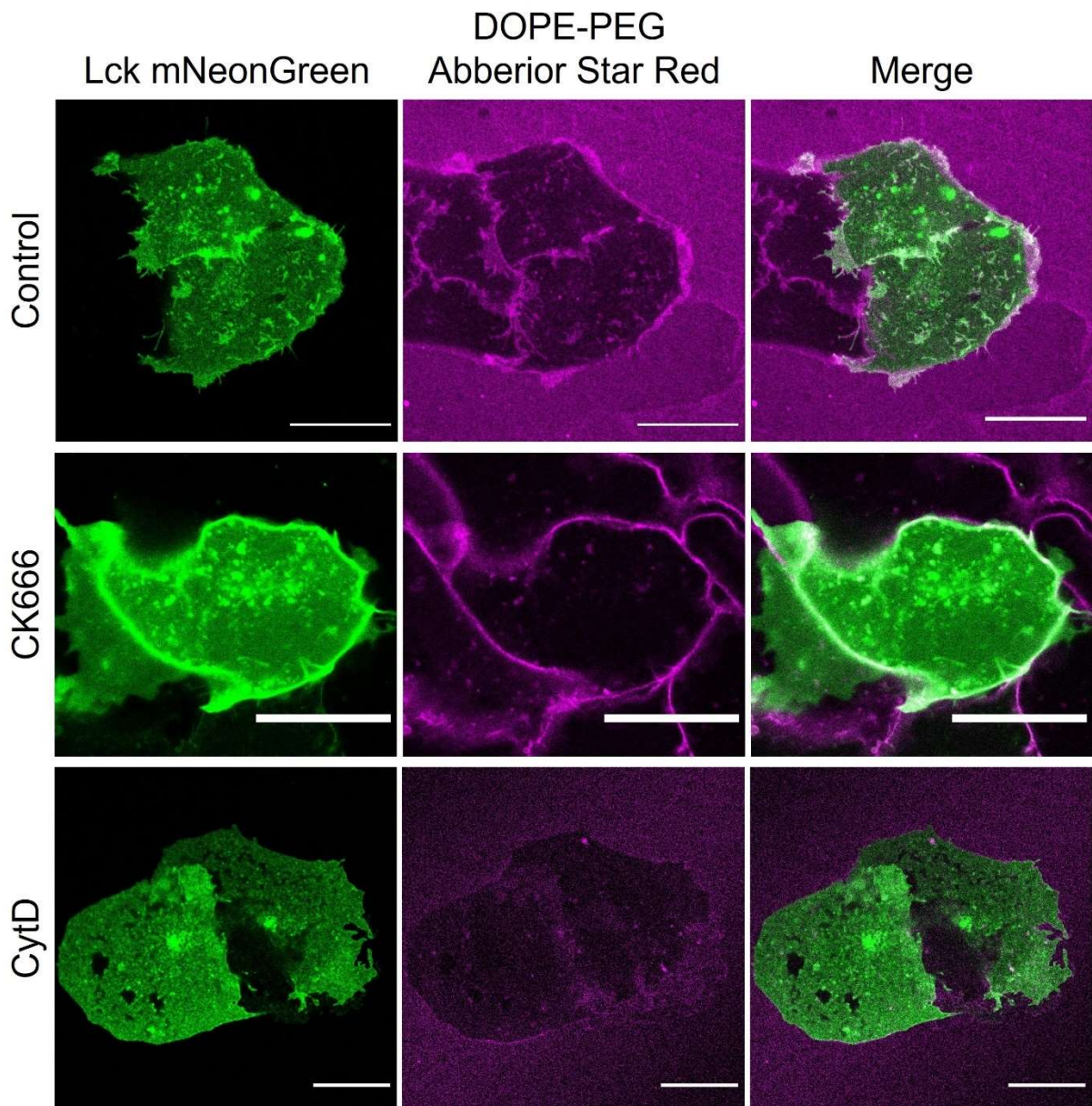


51. Wang LN, Gao MH, Wang B, Cong BB, Zhang SC. A role for GPI-CD59 in promoting T-cell signal transduction via LAT. *Oncol Lett.* 2018;15(4):4873-81.
52. Keller H, Lorizate M, Schwille P. PI(4,5)P2 degradation promotes the formation of cytoskeleton-free model membrane systems. *Chemphyschem : a European journal of chemical physics and physical chemistry.* 2009;10(16):2805-12.
53. Bruce Alberts AJ, Julian Lewis, Martin Raff, Keith Roberts, and Peter Walter. *Molecular Biology of the Cell*: Garland Publishing Inc; 2014.
54. Li Y, Yin Y, Mariuzza RA. Structural and biophysical insights into the role of CD4 and CD8 in T cell activation. *Front Immunol.* 2013;4:206-.
55. Wittlich M, Koenig BW, Hoffmann S, Willbold D. Structural characterization of the transmembrane and cytoplasmic domains of human CD4. *Biochimica et Biophysica Acta (BBA) - Biomembranes.* 2007;1768(12):2949-60.
56. Zhukovsky MA, Filograna A, Luini A, Corda D, Valente C. Protein Amphipathic Helix Insertion: A Mechanism to Induce Membrane Fission. *Frontiers in cell and developmental biology.* 2019;7:291-.
57. Sezgin E, Schwille P. Fluorescence techniques to study lipid dynamics. *Cold Spring Harbor perspectives in biology.* 2011;3(11):a009803.

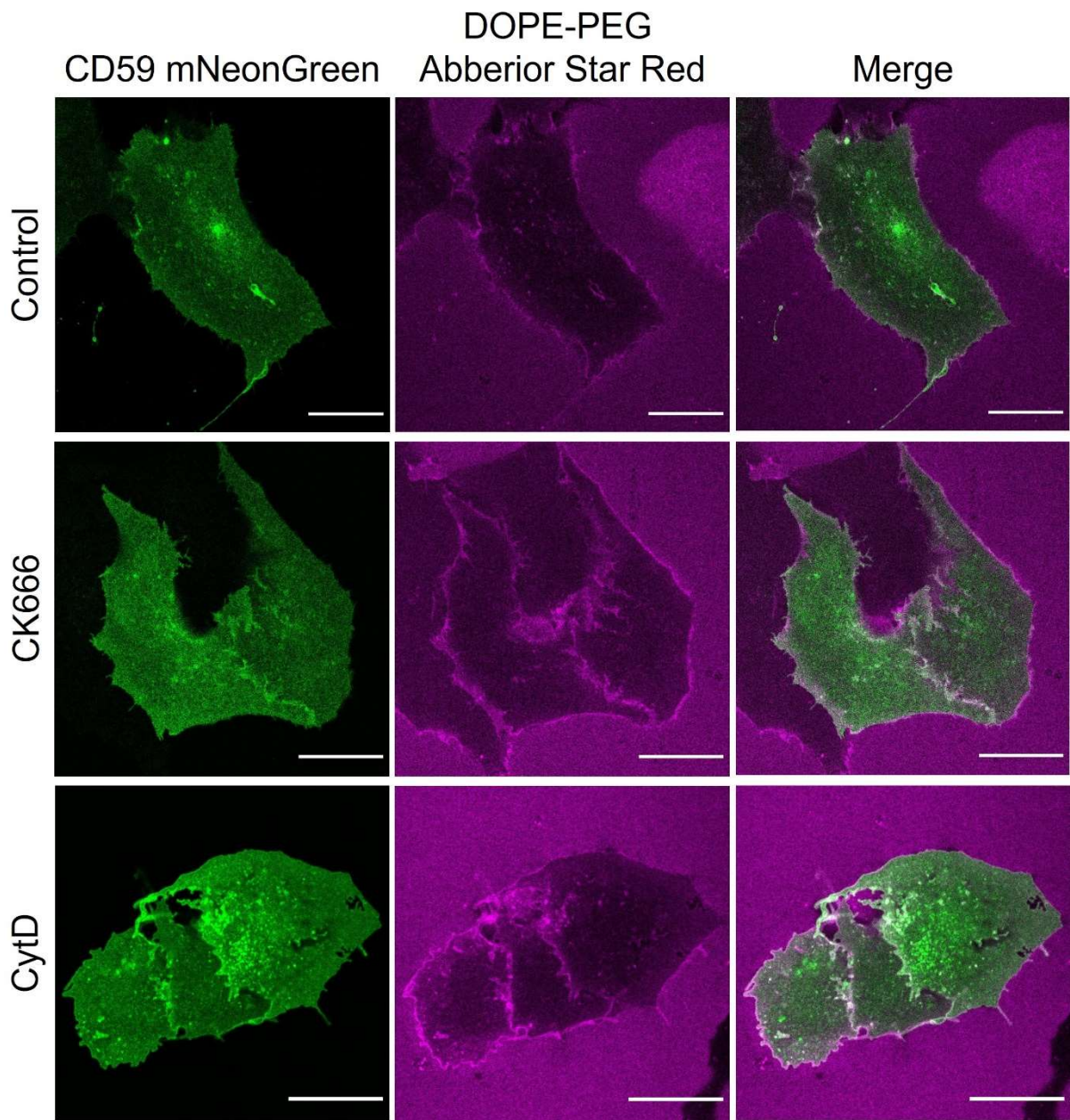
SUPPLEMENTARY FIGURES AND TABLES



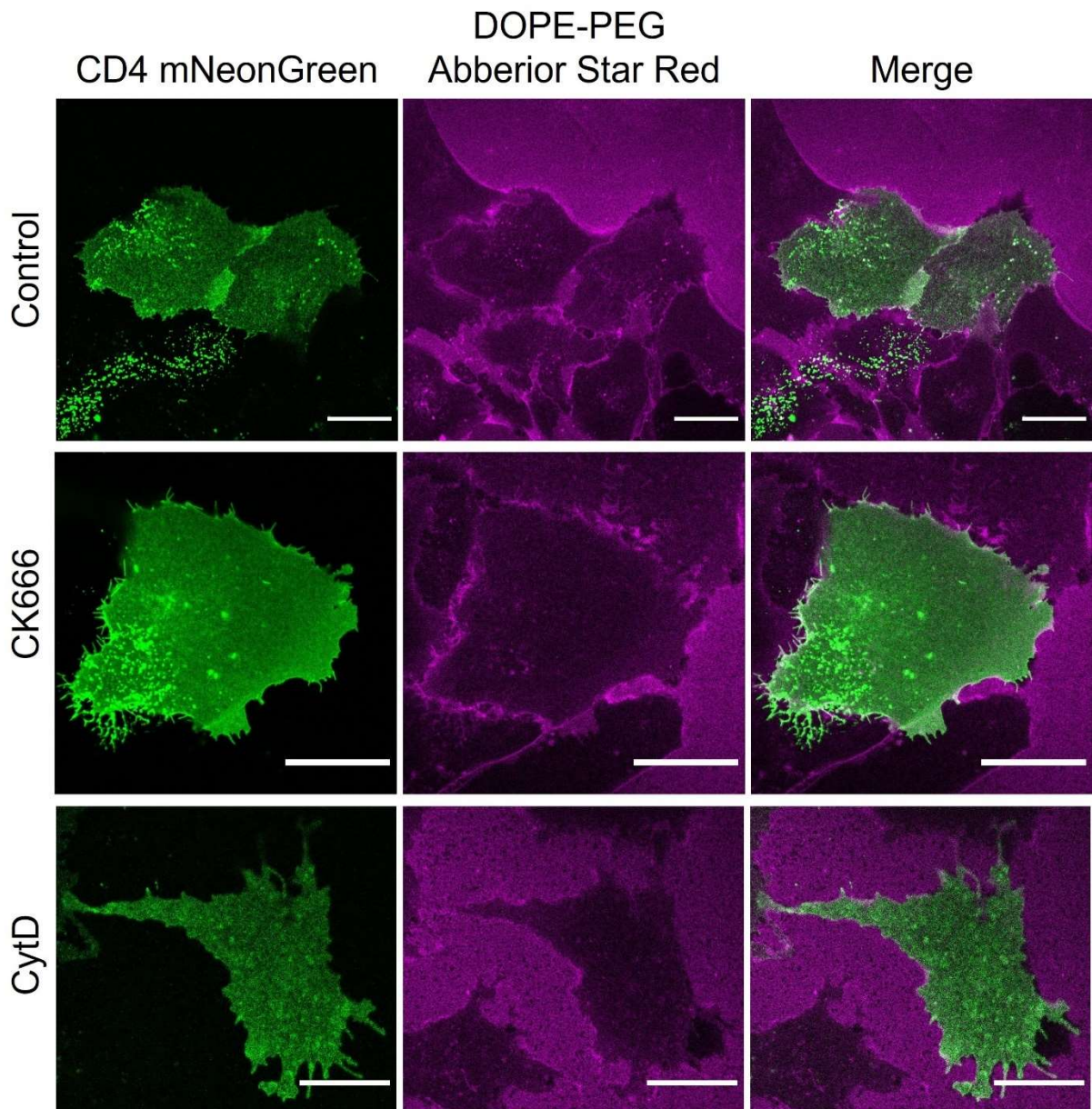
**Supplemental figure 1.** CHO cells are incompatible with the GPMV isolation protocol using NEM, rather than DTT and PFA.. Shown here are GPMVs produced with GPMV buffer supplemented with 0.5 (top), 1 (middle) or 2 (bottom) mM NEM. GPMVs produced with this protocol contained large concentrations of membrane protein within their lumen and contained highly uneven membrane surfaces. Depicted here are GPMVs isolated from cells were transfected with CD59-mNG, labelled with DOPE-PEG-ASR. Scale bar is 5  $\mu$ m.



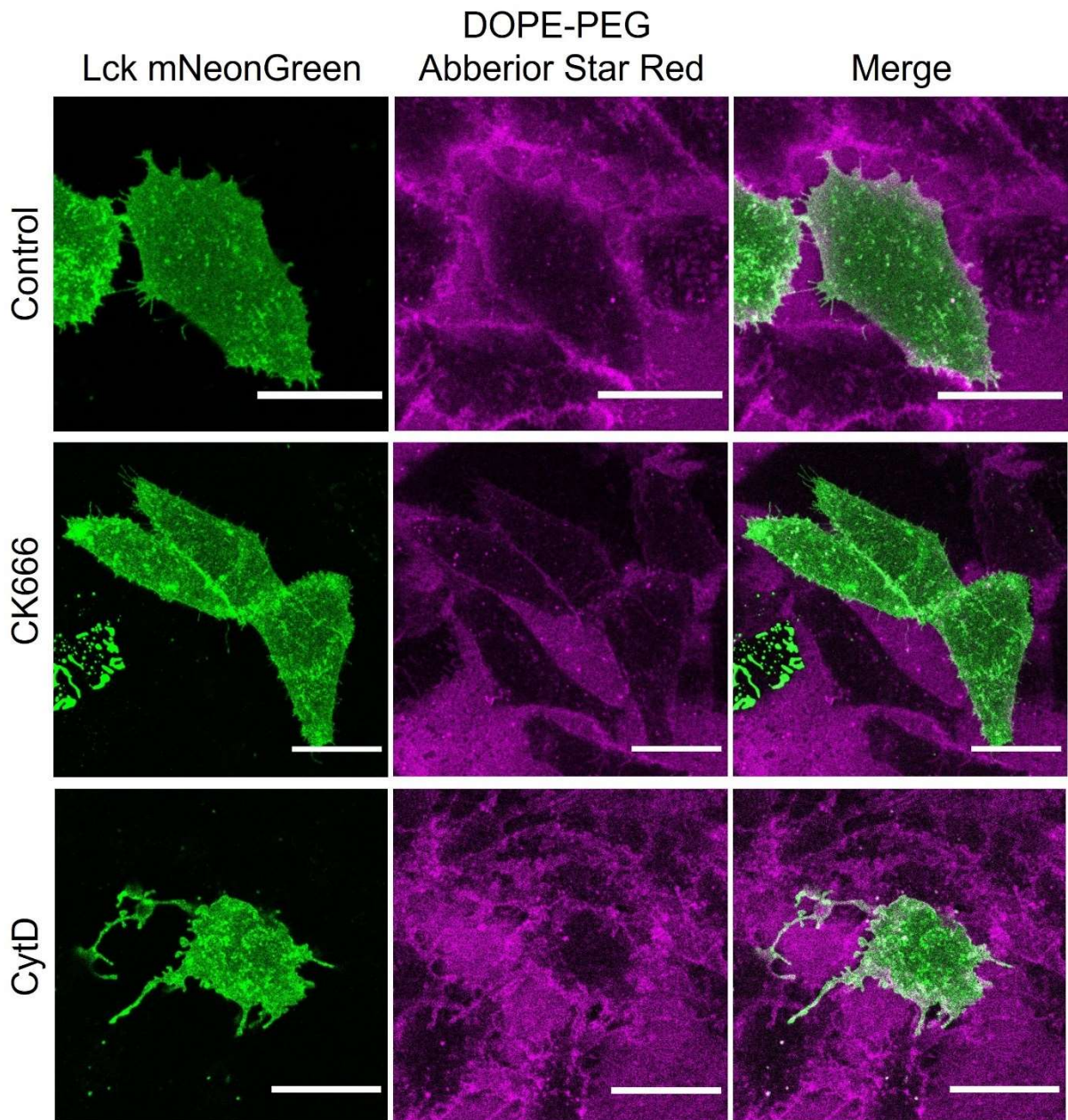
**Supplemental figure 2.** U2OS cells expressing Lck-mNG (green) labelled with DOPE-PEG-ASR (magenta), representative of FCS measured cell. Shown here is the plasma membrane at the cover glass interface, which was measured with FCS. Scale bar is 20  $\mu$ m.



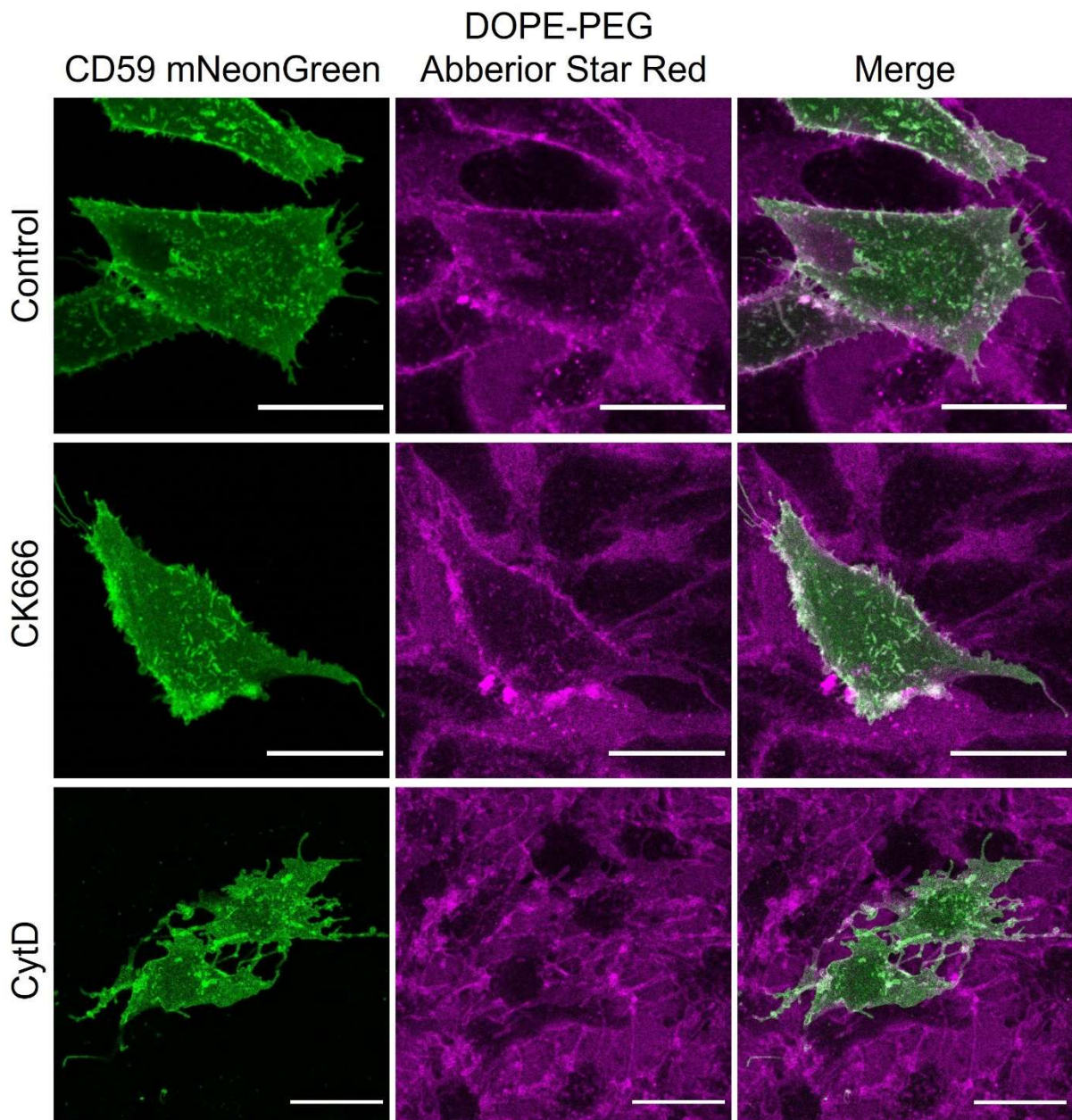
**Supplemental figure 3.** U2OS cells expressing CD59-mNG (green) labelled with DOPE-PEG-ASR (magenta), representative of FCS measured cell. Shown here is the plasma membrane at the cover glass interface, which was measured with FCS. Scale bar is 20  $\mu$ m.



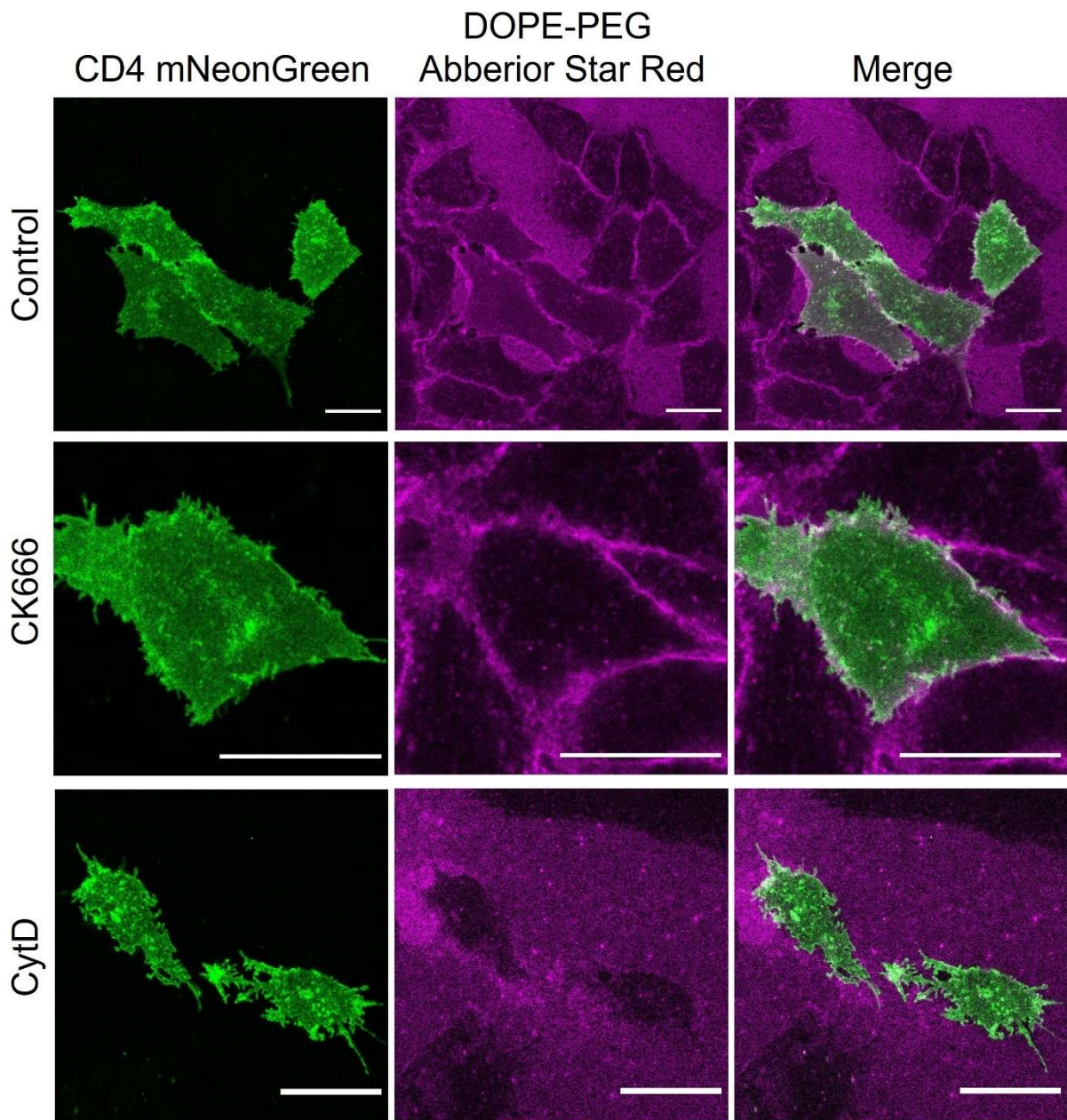
**Supplemental figure 4.** U2OS cells expressing CD4-mNG (green) labelled with DOPE-PEG-ASR (magenta), representative of FCS measured cell. Shown here is the plasma membrane at the cover glass interface, which was measured with FCS. Scale bar is 20  $\mu$ m.



**Supplemental figure 5.** CHO cells expressing Lck-mNG (green) labelled with DOPE-PEG-ASR (magenta), representative of FCS measured cell. Shown here is the plasma membrane at the cover glass interface, which was measured with FCS. Scale bar is 20  $\mu$ m.

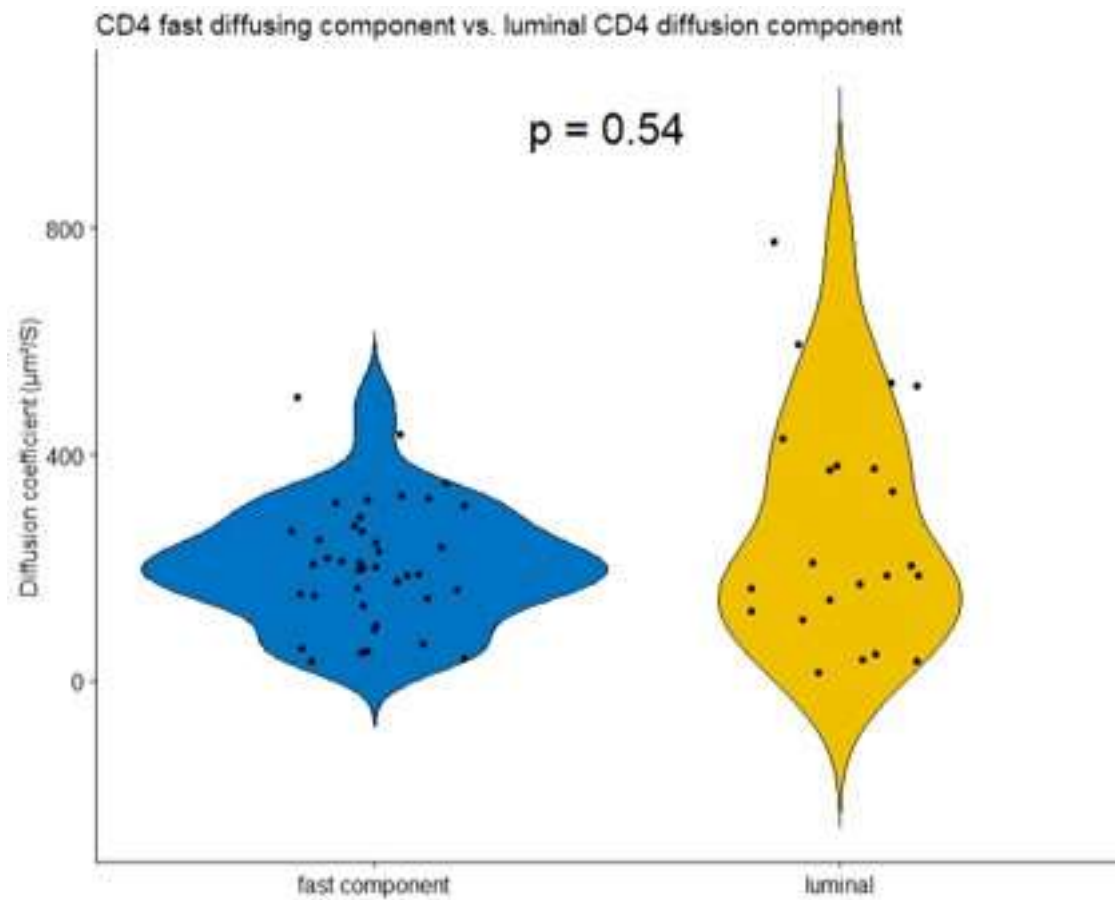


**Supplemental figure 6.** CHO cells expressing CD59-mNG (green) labelled with DOPE-PEG-ASR (magenta), representative of FCS measured cell. Shown here is the plasma membrane at the cover glass interface, which was measured with FCS. Scale bar is 20  $\mu\text{m}$ .

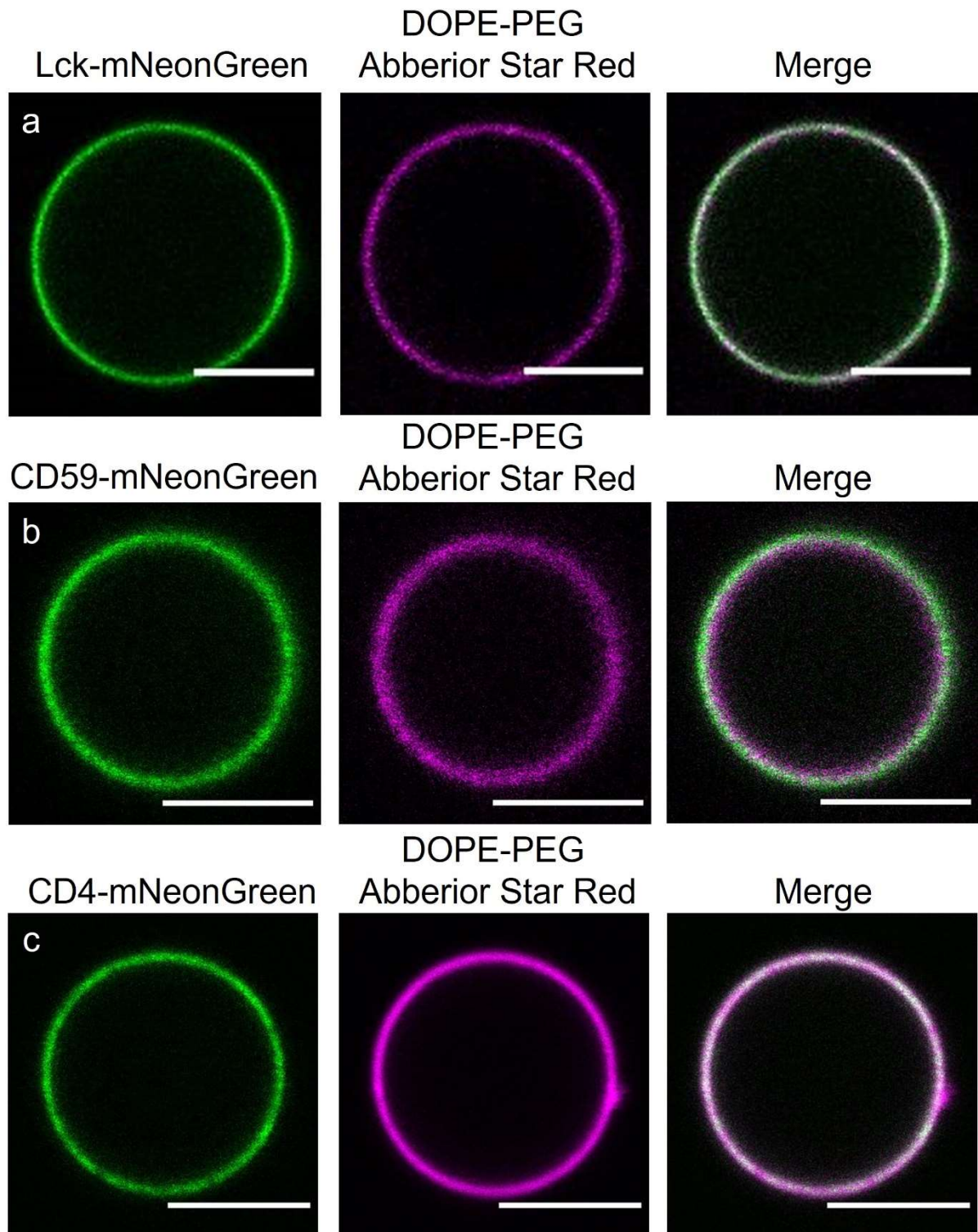


**Supplemental figure 7.** CHO cells expressing CD4-mNG (green) labelled with DOPE-PEG-ASR (magenta), representative of FCS measured cell. Shown here is the plasma membrane at the cover glass interface, which was measured with FCS. Scale bar is 20  $\mu\text{m}$ .

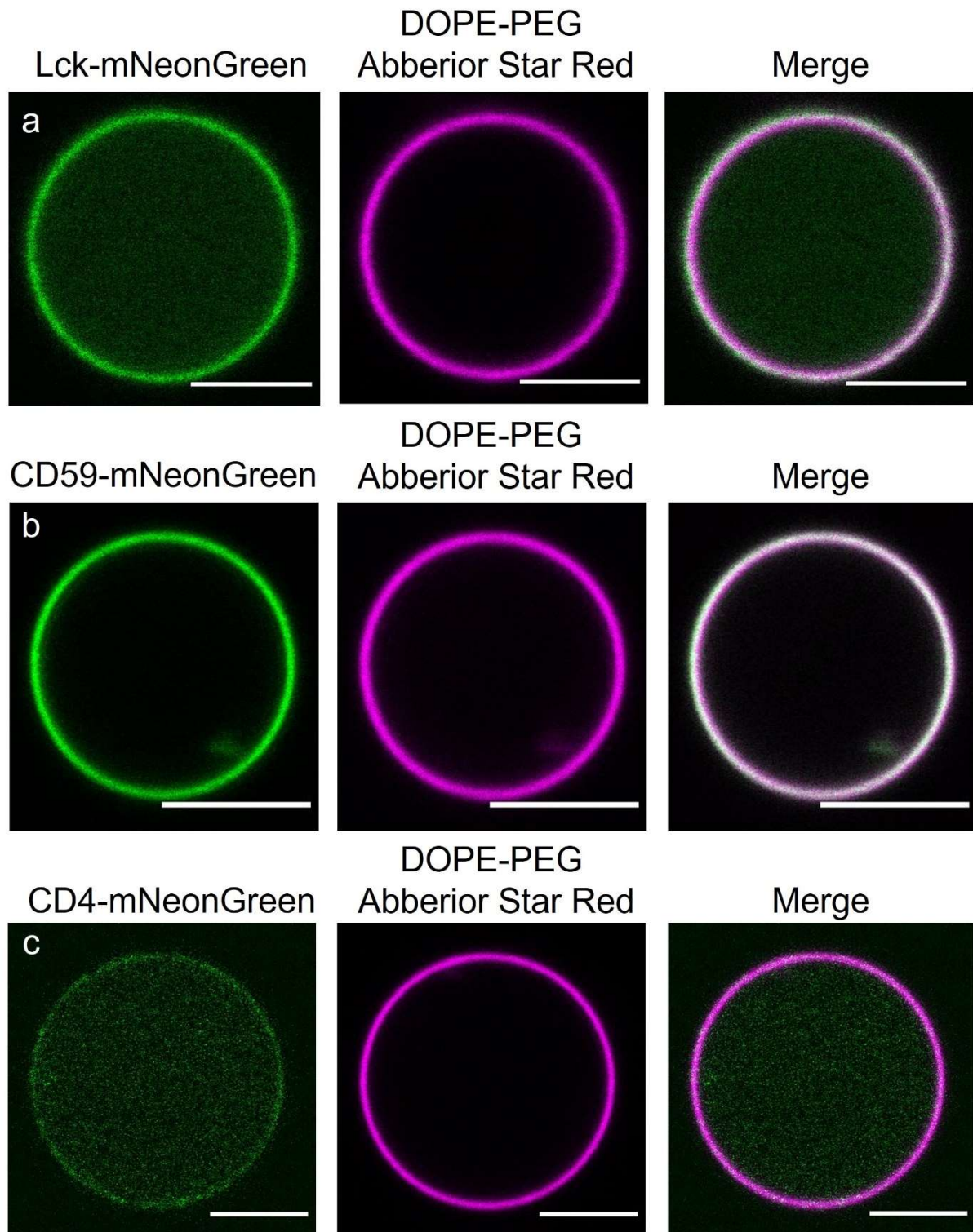




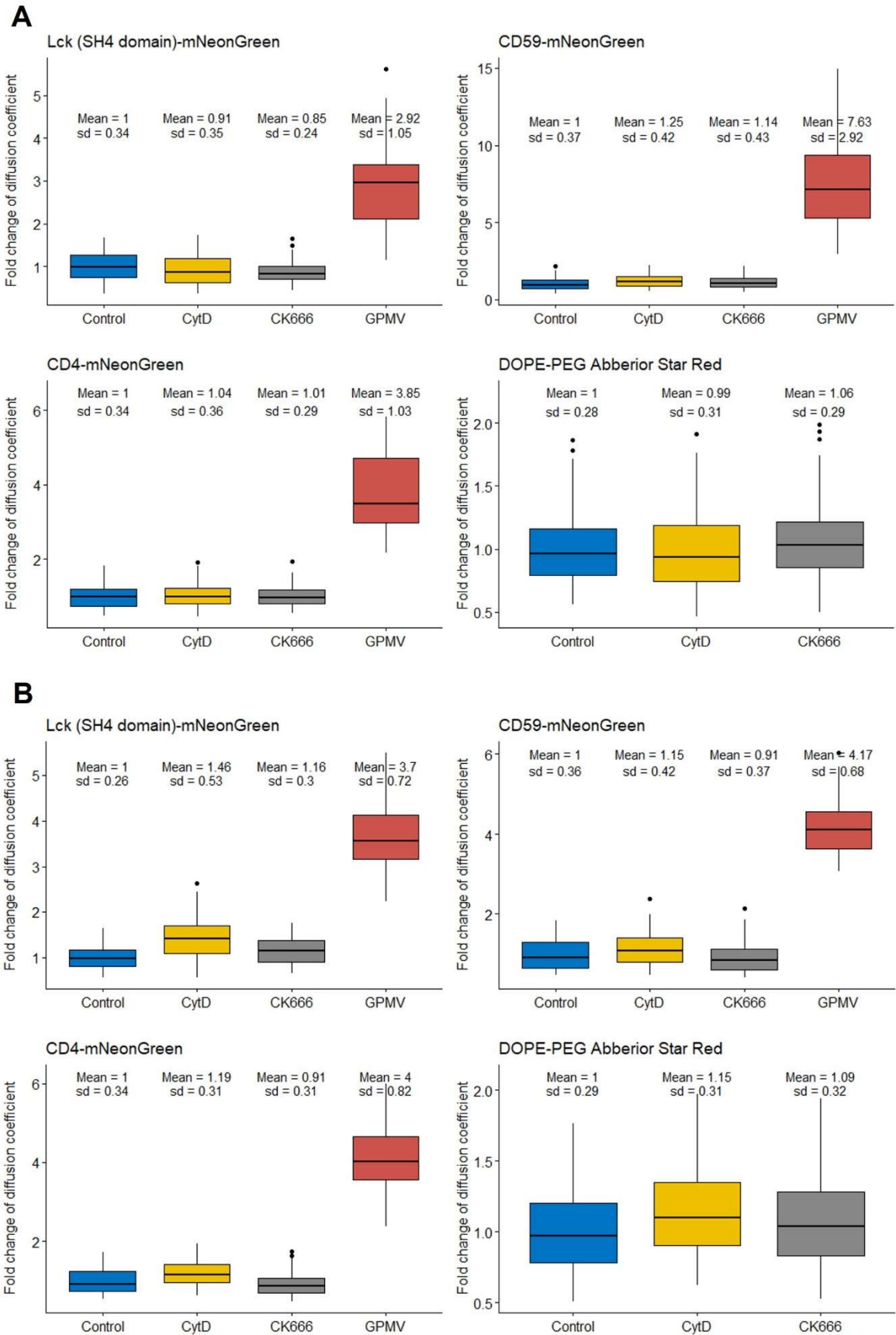
**Supplemental figure 8.** Comparison between the diffusion components of the fast moving component of CD4 detected in CHO-derived GPMV membranes and the diffusion components of CD4 measured in the lumen of CHO-derived GPMVs. Shown is a lack in difference in diffusion coefficient between these two groups, suggesting the fast component detected in measurements of GPMV membranes to be the luminal CD4.



**Supplemental figure 9.** GPMVs derived from U2OS cells expressing **(a)** Lck-mNeonGreen, **(b)** CD59-mNeonGreen and **(c)** CD4-mNeonGreen. All GPMV membranes were labelled with DOPE-PEG-ASR. Noteworthy is the homogenous distribution of the three imaged proteins, as the GPMVs lack the membrane clustering of Lck-mNeonGreen and CD4-mNeonGreen. Scale bar is 5  $\mu$ m.



**Supplemental figure 10.** GPMVs derived from CHO cells expressing (a) Lck-mNeonGreen, (b) CD59-mNeonGreen and (c) CD4-mNeonGreen. All GPMV membranes were labelled with DOPE-PEG-ASR. Noteworthy is the homogenous distribution of the three imaged proteins, as the GPMVs lack the membrane clustering of Lck-mNeonGreen, CD59-mNeonGreen, CD4-mNeonGreen. Furthermore, these GPMVs were isolated using DTT and PFA as vesiculation agents. This has resulted in a relatively large luminal presence of Lck-mNeonGreen and CD4-mNeonGreen. Scale bar is 5  $\mu$ m.



**Supplemental figure 11.** The diffusion coefficients of Lck-mNG, CD59-mNG, CD4-mNG and DOPE-PEG-ASR in live **(A)** U2OS and **(B)** CHO cells and cell-derived GPMVs, as determined by FCS, shown in fold change from control conditions.

Supplementary table 1. List of materials used in this study.

REAGENT OR RESOURCE	SOURCE	IDENTIFIER
Experimental cell models		
Chinese Hamster Ovary	Internal stock	RRID: CVCL_0213
U2OS	Internal stock	RRID: CVCL_0042
Chemicals		
1,4-dithiothreitol	Sigma Aldrich	3483-12-3
CK666	Sigma Aldrich	SML0006
Cytochalasin D	Sigma Aldrich	C8273
Dimethyl sulfoxide	Sigma Aldrich	D2438
DMEM, high glucose	ThermoFisher Scientific™	11965084
DMEM/F-12, HEPES	ThermoFisher Scientific™	11330057
DOPE-PEG labelled with Abberior Star Red	Abberior	N.A. (custom design)
Fetal Bovine Serum	Sigma Aldrich	F7524
Gibco™ PBS, pH 7.4	ThermoFisher Scientific™	15374875
Leibovitz's L-15 Medium, no phenol red	ThermoFisher Scientific™	21083027
N-ethylmaleimide	Sigma Aldrich	128287
Paraformaldehyde	Sigma Aldrich	30525-89-4
RPMI-1640 Medium	Sigma Aldrich	R8758
Trypsin-EDTA (0.05%), phenol red	ThermoFisher Scientific™	25300054
Critical Commercial Assays		
LB Broth (Miller)	Sigma Aldrich	L3522
LB Broth with agar (Miller)	Sigma Aldrich	L3147
Library Efficiency® DH5α™ Competent Cells	ThermoFisher Scientific™	18263012
Lipofectamine™ 3000 Transfection Reagent	ThermoFisher Scientific™	L3000015
NucBlue™ Live ReadyProbes™ Reagent (Hoechst 33342)	ThermoFisher Scientific™	R37605
ZymoPURE II Plasmid Midiprep Kit	Zymo Research	D4201
Plasmids		
CD59 mNeonGreen	Internal stock	N.A.
Endogenous SP-CD4 mNeonGreen	Internal stock	N.A.
LifeAct-mNeonGreen	Addgene	Plasmid #98877
Lymphocyte-specific protein tyrosine kinase (SH4 domain) mNeonGreen	Internal stock	N.A.